Food Chemistry 473 (2025) 143110

Contents lists available at ScienceDirect

Food Chemistry

journal homepage: www.elsevier.com/locate/foodchem

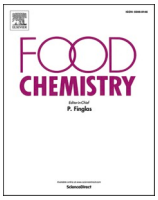

Understanding the molecular mechanism of fumonisin esterases by kinetic and structural studies

Dániel J. Incze [a,b], Zsófia Molnár [a,c], Gergely N. Nagy [c,d], Ibolya Leveles [c,d], Beáta G. Vértessy [c,d], László Poppe [a,e,*], Zsófia Bata [b,*]

[a] Department of Organic Chemistry and Technology, Faculty of Chemical Technology and Biotechnology, Budapest University of Technology and Economics, Műegyetem rkp. 3, Budapest 1111, Hungary
[b] Dr. Bata Ltd., Research and Development Laboratory, Bajcsy-Zsilinszky u. 139, Ócsa 2364, Hungary
[c] Institute of Molecular Life Sciences, HUN-REN, Research Centre for Natural Sciences, Magyar Tudósok krt. 2, Budapest 1117, Hungary
[d] Department of Applied Biotechnology and Food Science, Faculty of Chemical Technology and Biotechnology, Budapest University of Technology and Economics, Műegyetem rkp. 3, Budapest 1111, Hungary
[e] Biocatalysis and Biotransformation Research Center, Faculty of Chemistry and Chemical Engineering, Babeş-Bolyai University of Cluj-Napoca, Arany János str. 11, Cluj-Napoca 400028, Romania

ARTICLE INFO

Keywords:
Fumonisin esterase
Fumonisin B_1
Enzyme mechanism
Acyl migration
Mycotoxin
Protein crystallography
Chemical compounds:
Fumonisin B_1 (PubChem CID: 2733487)
Hydrolyzed Fumonisin B_1 (PubChem CID: 15875284)
Fumonisin B_1 esterase (SID: 405229404)

ABSTRACT

Fumonisins are sphingolipid-like mycotoxins that cause serious damage by contaminating food and feed. The tricarballylic acid (TCA) units of fumonisin B_1 (FB_1; accounting for 70 % of fumonisin contamination) can be removed by fumonisin B_1 esterase (FE, EC 3.1.1.87) providing a biotechnological FB_1 detoxification possibility. Here, we report the regioselective cleavage of the TCA ester at C6 in the first step of FB_1 hydrolysis and kinetic characterization for two FEs. The low K_M values (4.76–44.3 μM) are comparable to concentrations of environmental contaminations, and the high catalytic efficiencies are promising for practical applications. The X-ray structure of one of the FEs enabled the understanding of the FB_1 hydrolysis at molecular level and revealed an arginine pocket key for substrate binding, and the catalytic role of the glutamate preceding the catalytic serine. Computations showed that this FE is likely capable of detoxifying any fumonisin indicating its potential applicability in food and feed products.

1. Introduction

Mycotoxins are toxic secondary metabolites of various moulds (fungi). The moulds grow on various crops and foodstuffs including cereals, nuts, and spices (WHO, 2023). Acute and chronic dietary exposures to mycotoxins induce mycotoxicosis, with adverse health effects in humans and livestock (Eskola et al., 2020). Fumonisins—primarily produced by *Fusarium verticillioides* and *Fusarium proliferatum*—are among the most frequently occurring mycotoxins that pose several health risks, primarily affecting the liver, kidneys, brain, and respiratory and immune systems through disruptions in sphingolipid metabolism (Riley & Merrill, 2019; Zhang et al., 2024). Fumonisins are classified into A, B, C, and P series (FA, FB, FC, FP, respectively)(Rheeder et al., 2002), with the most toxic and prevalent among them being Fumonisin B_1 (FB_1, Fig. 1), which causes 70 % of fumonisin contaminations (Chen et al., 2021; Kamle et al., 2019). A comprehensive study between 2006 and 2016 on raw cereal grains worldwide showed detectable levels of FB_1 in 61 % of the samples, with a maximum concentration of 98.53 μM (71.12 ppm) (Lee & Ryu, 2017).

Elimination of FB_1 contamination is a great challenge in the food and feed industries. FB_1 has remarkable chemical stability, and its decomposition can be only achieved when heated above 150–200 °C (Humpf & Voss, 2004) or under strongly alkaline conditions (Sydenham, Stockenstrom, et al., 1995). Physical (sorting, washing, irradiation, adsorbents) or chemical (alkaline- or ozone-) treatments are either not effective enough, or lower the nutritional value of the food, or else are not applicable for food decontamination on an industrial scale (Liu et al., 2022). Enzymatic detoxification has emerged as a promising approach

* Corresponding authors at: Budapest University of Technology and Economics, Műegyetem rkp. 3, Budapest 1111, Hungary (L. Poppe). Dr. Bata Ltd., Bajcsy-Zsilinszky u. 139, Ócsa H-2364, Hungary (Z. Bata).
E-mail addresses: poppe.laszlo@vbk.bme.hu (L. Poppe), sbata@drbata.com (Z. Bata).

https://doi.org/10.1016/j.foodchem.2025.143110
Received 14 August 2024; Received in revised form 19 January 2025; Accepted 25 January 2025
Available online 27 January 2025

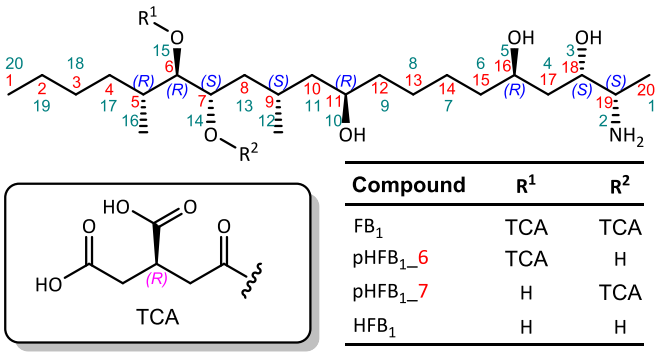

Compound	R^1	R^2
FB_1	TCA	TCA
$pHFB_1$_6	TCA	H
$pHFB_1$_7	H	TCA
HFB_1	H	H

IUPAC Names

FB_1: (2*R*)-2-[2-[(5*R*,6*R*,7*S*,9*S*,11*R*,16*R*,18*S*,19*S*)-19-amino-6-[(3*R*)-3,4-dicarboxybutanoyl]-oxy-11,16,18-trihydroxy-5,9-dimethylicosan-7-yl]-oxy-2-oxoethyl]butanedioic acid

$pHFB_1$_6: (2*R*)-2-[2-[(5*R*,6*R*,7*S*,9*S*,11*R*,16*R*,18*S*,19*S*)-19-amino-7,11,16,18-tetrahydroxy-5,9-dimethylicosan-6-yl]oxy-2-oxoethyl]butanedioic acid

$pHFB_1$_7: (2*R*)-2-[2-[(5*R*,6*R*,7*S*,9*S*,11*R*,16*R*,18*S*,19*S*)-19-amino-6,11,16,18-tetrahydroxy-5,9-dimethylicosan-7-yl]oxy-2-oxoethyl]butanedioic acid

HFB_1: (2*S*,3*S*,5*R*,10*R*,12*S*,14*S*,15*R*,16*R*)-2-amino-12,16-dimethylicosane-3,5,10,14,15-pentaol

Fig. 1. Fumonisin B_1 and its degradation products by fumonisin B_1 esterase. FB_1, Fumonisin B_1; $pHFB_1$_6, partially hydrolyzed Fumonisin B_1 esterified at the C6 position; $pHFB_1$_7, partially hydrolyzed fumonisin B_1 esterified at the C7 position; HFB_1, hydrolyzed fumonisin B_1; TCA, tricarballylic acid. The numbering of the general structure in red follows the IUPAC nomenclature of FB_1, $pHFB_1$_6 and $pHFB_1$_7, while the numbers in green follow the IUPAC naming of HFB_1. Configurations of centers of asymmetry (*R*) and (*S*) are indicated. (For interpretation of the references to colour in this figure legend, the reader is referred to the web version of this article.)

for post-harvest decontamination of FB_1 with increased efficiency at milder treatment conditions.

Fumonisin B_1 esterases (FE, EC 3.1.1.87) catalyze the ester hydrolysis of FB_1 at the C6 and C7 positions, resulting in an aminopentol (hydrolyzed FB_1, HFB_1) and two tricarballylic acid (TCA) molecules as final products (Fig. 1). Several available *in vivo* studies carried out in laboratory species point to a lower toxicological significance of HFB_1 compared to FB_1. Based on plasma and liver sphinganine/sphingosine (Sa/So) ratios (which were taken as a biomarker of FB_1 toxicity), liver and enteric morphology, and cytokine expression, a much lower effect of HFB_1 compared to FB_1 was documented in piglets fed a diet of contaminated feed for 14 days (Grenier et al., 2012). Similar results were found in turkeys and piglets as well, concerning the influence of FB_1 and HFB_1 on the Sa/So ratio. (Masching et al., 2016). These results reinforce the view that FB_1 hydrolysis should be considered as a detoxification mechanism (EFSA Panel on Contaminants in the Food Chain et al., 2018).

Currently, only a few FEs have been described: *Sphingopyxis macrogoltabida* MTA144 (termed here as FE1) (Heinl et al., 2010), *Caulobacter* sp. ATCC 55552 (FE2)(Duvick et al., 1998), *Exophiala spinifera* ATCC 74269 (FE3)(Duvick et al., 1998), *Rhinocladiella atrovirens* ATCC 74270 (Duvick et al., 1998), and the protein coded by the gene KUO56785 of *Sphingomonadales bacterium* (FE4)(Li et al., 2021). Based on their amino acid sequences, all FEs are α/β hydrolases and possess the canonical Ser-His-Glu(Asp) triad as the catalytic machinery typical for serine esterases. Due to the presence of both partially hydrolyzed FB_1 regioisomers ($pHFB_1$_6 and $pHFB_1$_7, Fig. 1) in FE enzymatic reaction samples, the FE-catalyzed hydrolysis was assumed to proceed through either of these intermediates (Humpf & Voss, 2004; Heinl et al., 2010; Masching et al., 2016; Neckermann et al., 2022; Hahn et al., 2015; Grenier et al., 2017; Schwartz-Zimmermann et al., 2018). However, an unexplored work in 1995 showed that the two $pHFB_1$ regioisomers underwent rearrangements at an elevated temperature (70 °C, 3 h) in an aqueous solution (Sydenham, Stockenstrom, et al., 1995). This raises the possibility that heat treatment during sample processing (Liu et al., 2022; Heinl et al., 2010; Masching et al., 2016; Neckermann et al., 2022; Hahn et al., 2015; Grenier et al., 2017; Schwartz-Zimmermann et al., 2018) may have influenced the samples' $pHFB_1$_6 and $pHFB_1$_7 content. Despite extensive studies of FEs, understanding their enzymatic mechanism remains incomplete.

Here, we provide a comprehensive kinetic and structure-based elucidation of the mycotoxin hydrolysis mechanism of FEs. Our rigorous kinetic investigations demonstrate that the two-step enzymatic hydrolysis of FB_1 by FE1 and FE2 selectively proceeds through the $pHFB_1$_7 intermediate. We further explore the complete kinetic characterization of the two FEs and the conditions and kinetics of equilibration of the $pHFB_1$ regioisomers to reflect on their relevance in practical decontamination applications. We additionally present the crystal structure of FE2, which sheds light on the fundamental aspects of the enzymatic specificity of FEs. We complemente the structural data with extensive *in silico* analyses to reveal catalytically relevant substrate binding conformations. Docking of a panel of FA/FB/FC/FP fumonisins in the FE2 active site indicates it to be a broad-specificity fumonisin esterase. Understanding the structural basis of substrate specificity can accelerate the discovery and engineering of FEs, contributing to the development of the application of this biocatalyst to enhance food safety.

2. Materials and Methods

2.1. Reagents, solvents, and analytical standards

Methanol (MeOH), water (H_2O), ethyl acetate (EtOAc), dimethyl sulfoxide (DMSO), and methanol-d_4 (all LC grade), as well as dichloromethane (DCM), glacial acetic acid (AcOH), concentrated hydrochloric acid solution (cc. HCl), all reagents for culture media and derivatization, buffer salts, silica resin, and bovine serum albumin (BSA) were purchased from either Reanal Laborvegyszer Kft. (Budapest, Hungary) or Merck KGaA (Darmstadt, Germany). Zeocin and SYPRO Orange Protein Stain were purchased from Thermo Fisher Scientific (Waltham, MA, USA). Biotage Isolute® C18 500 mg/6 mL solid phase extraction (SPE) columns were purchased from Simkon Kft. (Budapest, Hungary). Analytical standards of FB_1 and HFB_1 were purchased from Cayman Chemical (Ann Arbor, MI, USA) and FERMENTEK Ltd. (Jerusalem, Israel), respectively.

2.2. Strains, plasmids, and enzyme production

Fusarium verticillioides NCAIM F.00935 was purchased from the National Collection of Agricultural and Industrial Microorganisms (Budapest, Hungary).

The nucleic acid sequences of FE1 (amino acid sequence at UniProt: D2D3B6, amino acids 48–540) and FE2 (Incze et al., 2023) were codon optimized based on *P. pastoris* codon bias, and purchased from ATUM (Newark, CA, USA) cloned into pD912 vectors. In these plasmids, recombinant protein production is driven by the AOX1 promoter, and the secretion signal, derived from the yeast mating pheromone alpha-factor of *Saccharomyces cerevisiae*, facilitates the secretion of heterologous proteins. The production plasmids of FE1 and FE2 were transformed into in-house prepared chemically competent *Escherichia coli* DH5α cells, according to the Hanahan method (Green & Sambrook, 2018). The transformed *E. coli* cells were selected on LB agar (0.5 % *w/v* yeast extract, 1 % w/v tryptone, and 1 % w/v sodium chloride, 1 % w/v bacteriological agar) supplemented with 25 μg mL^{-1} Zeocin. LB medium with 25 μg mL^{-1} Zeocin was used for plasmid amplification. The plasmids were isolated with the EZ-10 Spin Column Plasmid DNA Kit (Bio Basic Canada Inc., Ontario, Canada), according to the manufacturer's protocol. *Pichia pastoris* strain PPS-9010 (ATUM, Newark, CA, USA) was

used as eukaryotic hosts for gene expression. Plasmid linearization with *Pme*I restriction enzyme (New England Biolabs, Ipswich, MA), electrocompetent *P. pastoris* cell production, transformation, selection, and protein production were performed according to ATUM's protocol (ATUM, 2017). FE1 and FE2 were secreted into the production media, and at the end of the production, the fermentation supernatant was evaluated for enzyme purity, protein concentration, and fumonisin esterase activity. The purity of the enzymes in the fermentation supernatant was assessed by sodium dodecyl sulfate-polyacrylamide gel electrophoresis (SDS-PAGE), using 4–15 % Mini-PROTEAN® TGX™ Precast Protein Gels (Bio-Rad, Hercules, CA, USA). Protein concentrations were measured with Bradford Reagent (Sigma-Aldrich, St. Louise, MO, USA), using a BSA solution for calibration. The results are shown in Fig. S21.

2.3. Production and purification of fumonisin B_1

Fusarium verticillioides NCAIM F.00935 was propagated in 400 mL of medium—containing 1 % *w/v* molasses and 3 % w/v yeast extract—in a 1-L Erlenmeyer flask for two days at 30 °C, by shaking at 90 rpm. Whole corn kernel (800 g) was mixed with water (130 mL), autoclaved twice at 121 °C for 30 min, and inoculated with the 400 mL of *F. verticillioides* culture. The solid-state fermentation was incubated at room temperature for six weeks, then air-dried and milled with a standard electronic mill. Finally, 0.5 g of sample was extracted with 2 × 5 mL of Extraction Solvent A (ACN: MeOH: H_2O, 25:25:50) and shaken for 2 × 20 min at room temperature at 100 rpm. The sample was centrifuged, and the extract was removed. The supernatants were combined and loaded onto a C18 SPE column that was prewashed with 5 mL of MeOH and 5 mL of H_2O subsequently. The column was washed sequentially with 5 mL of H_2O, 5 mL of Extraction Solvent B (MeOH: H_2O, 1:3), and then finally eluted with 2 mL of MeOH. The concentration of FB_1 in the eluate was determined by HPLC, as described in Section 2.4.

Dried culture material (800 g, containing 210 mg kg^{-1} of FB_1) was extracted consecutively with 1600 mL and 800 mL of Extraction Solvent B for 15 min, and the solid material was separated by centrifugation at 15,650 *g* for 5 min. The supernatant was decanted from the pellet, and the supernatant's p*H* was adjusted to 2 with 5 M HCl solution to precipitate the dissolved proteins. The solution was centrifuged again; then the decanted supernatant was filtered through a paper filter. The supernatant (~1600 mL, containing 160 mg of FB_1) was passed through a C18 SPE column in 15 mL aliquots (prewashed with 5 mL of MeOH and 5 mL of H_2O) and then washed sequentially with 5 mL of H_2O, 5 mL of Extraction Solvent B, and then finally eluted with 4 mL of MeOH, without any significant loss of the FB_1 quantity. The eluted aliquots were combined, and the MeOH was evaporated with a vacuum rotary evaporator. The oily, dark brown residue was dissolved in 50 mL of H_2O, and the p*H* was adjusted to 4.5. The solution was extracted with EtOAc (4 × 10 mL) to remove the apolar contaminants; then the aqueous phase was evaporated to dryness with a vacuum rotary evaporator to leave an oily, light brown material.

The oily, light brown material was dissolved in 10 mL of MeOH and dried onto 5 g of Kieselgel 60 (63–200 μm) by a vacuum rotary evaporator. Column chromatography was performed on 100 g of Kieselgel 60 with Eluent C (DCM:MeOH:AcOH:H_2O, 55:36:8:1), as previously described (Sydenham, Stockenstrom, et al., 1995). The fractions containing FB_1 were combined and evaporated to dryness with a rotary evaporator. The residue, containing 155 mg of FB_1, was dissolved in 10 mL of Eluent D (MeOH:50 mM potassium-phosphate buffer (p*H* 5.0), in a 60:40 ratio) and filtered through a 0.22 μm syringe filter. The contaminants and FB_1 were separated using an EX-1600 HPLC instrument (Exformma Technologies Ltd., Kowloon, Hong Kong) on a Supelco SUPERCOSIL PLC-18 (25 cm × 21.2 mm, 12 μm) column (Merck KGaA) in 1 mL portions (10 runs) using UV detection at 200 nm. The separation was performed at 30 °C at a flow rate of 5 mL min^{-1}. Most contaminants eluted between 11 and 15 min, while partially purified FB1 eluted between 14 and 21 min. Fractions 15–20, containing 170 mg of partially purified FB_1, were combined and evaporated to dryness with a rotary evaporator. The residue was dissolved in 20 mL of Eluent A and applied onto Phenomenex Gemini-NX C18 (250 mm × 10 mm, 110 Å, 5 μm) column in 0.5 mL portions (40 runs on EX-1600 with column incubation at 15 °C, using Eluent A at a flow rate of 2 mL min^{-1} with fraction collection change in every minute). Fractions 13–14 from all runs, containing 48 mg of FB_1, were concentrated on a C18 SPE column as described above, and the combined concentrates were evaporated to dryness with a vacuum rotary evaporator.

2.4. General analysis of samples containing FB_1 and its metabolites, by HPLC-FLD

The *o*-phthalaldehyde (OPA) derivatization procedure, HPLC separation, and fluorescent detection of the derivatized analytes used in this study were based on a previous work (Shephard et al., 1994) with minor modifications. HPLC equipped with a fluorescent detector (FLD) served to quantify FB_1 and metabolites throughout the study. If not indicated otherwise, the samples were diluted or dissolved in MeOH. A sample solution of 10 μL was mixed with 10 μL of OPA reagent (40 mg of *o*-phthalaldehyde and 50 μL of β-mercaptoethanol in 1 mL of MeOH and 5 mL of 0.1 M $Na_2B_4O_7$ solution) and kept for 5 min at 20 °C before injection. The derivatized analytes were separated on a reverse phase C18 column (Kinetex, 2.6 μm, C18, 100 Å, 100 × 4.6 mm) (Phenomenex, Torrence, CA, USA) in a Shimadzu CTO-40C column thermostat (Shimadzu Corporation, Kyoto, Japan) at 30 °C, and analyzed with a Shimadzu HPLC device coupled to a fluorescent detector (Shimadzu RF-20 A XS, extension wavelength of 335 nm, emission wavelength of 440 nm). During HPLC separation with Shimadzu LC-40D XR the mobile phase was pumped at a flow rate of 0.75 mL min^{-1}. Initially, pure Eluent A (MeOH: 50 mM sodium phosphate buffer (p*H* 5.0), 65:35) was pumped for 5 min, followed by a linear gradient of Eluent B up to 70 % (HPLC-grade methanol) within 9 min. Finally, the column was re-equilibrated for 3 min with 100 % of Eluent A. The concentration of FB_1 and HFB_1 was determined from standard calibrations. FB_1 and HFB_1 showed the same molar response factor, as the signal originated from the OPA derivate, which was formed with the molecules' amino group and seemingly independent of the presence of the TCA groups. Therefore, the same molar response factors were applied to calculate $pHFB_1$_7 and $pHFB_1$_6 concentrations.

2.5. Enzyme activity evaluation of the fermentation supernatant

All substrate and enzyme solutions were diluted for the enzyme activity measurements in buffer A (50 mM potassium-phosphate buffer supplemented with 100 μg mL^{-1} BSA, at p*H* 6.0). Analytical standard FB_1 solution was diluted to a final concentration of 100 mg L^{-1}. The enzymatic reaction was carried out in a 200 μL plastic tube, with 72.2 μL of the FB_1 solution, 7.8 μL of buffer A, and 20 μL of enzyme solution. Prior to the reaction, the crude fermentation supernatant was diluted to a concentration that resulted in a conversion of less than 20 % in the enzyme reaction in 15 min. The reaction mixtures were incubated at 37 °C in a TDB-120 Dry Block Thermostat (Biosan, Riga, Latvia) for 15 min and the reactions were terminated by boiling for 5 min at 100 °C. The reactions were diluted 10-fold in Eluent A (MeOH: sodium phosphate buffer (p*H* 5.0), 65:35) and analyzed with HPLC-FLD. Alternatively, the reactions were terminated by mixing 20 μL of the reaction mixture with 180 μL of MeOH.

2.6. Enzymatic production of $pHFB_1$ and HFB_1 and their purification

$pHFB_1$s are not available commercially either in a pure form or as a mixture. The two regioisomers of $pHFB_1$—denoted as $pHFB_1$a and $pHFB_1$b without structure assignation—were separated earlier by preparative HPLC (Hahn et al., 2015; Schwartz-Zimmermann et al., 2018).

The $pHFB_1$ and HFB_1 materials were prepared by enzymatic degradation of FB_1 in two separate reactions. FB_1 was obtained by fermentation and multi-step purification. The purified FB_1 was dissolved in 50 mM potassium phosphate buffer at p*H* 6.0 to reach a final FB_1 concentration of 277.1 μM. To prepare $pHFB_1$, an enzyme solution (6 μL, containing 202 mg L^{-1} of FE1) was added to the FB_1 solution (60 mL, 277.1 μM), and the resulting mixture was incubated at 37 °C for 15 min. The p*H* of the reaction mixture was adjusted to 2, to terminate the enzymatic hydrolysis. For the preparation of HFB_1, the reaction was carried out similarly, except for elongating the reaction time by 1 h to reach the complete hydrolysis. The reaction mixtures were purified and concentrated with C18 SPE columns and separated with HPLC on the Phenomenex Gemini-NX C18 column, (250 mm × 10 mm, 110 Å, 5 μm) column in 0.5 mL portions (40 runs on EX-1600 with column incubation at 15 °C, using Eluent A at a flow rate of 2 mL min^{-1} with fraction collection change in every minute). Fractions containing high concentrations of the target compounds were diluted with H_2O to obtain 75 % H_2O content and acidified to p*H* 2.0 with 5 M HCl, then subsequently concentrated again with C18 SPE columns as described above, lyophilized, and stored at −20 °C until further use.

2.7. ^1H NMR measurements on FB_1, $pHFB_1$, and HFB_1

The NMR spectra were recorded in MeOH-d_4 on a Bruker Avance DRX500 spectrometer operating at 500 MHz for ^1H, and signals are given in ppm on the δ scale (^1H NMR in MeOH-d_4: δ 3.32 ppm, or D_2O: δ = 4.86). Splitting patterns are designated as *dd*, doublet of doublets; *ddd* doublet of doublet of doublets; *m*, multiplet. Spin-spin coupling constants (*J*) were given in Hz units. Assignments of the signals are shown in Supporting Information Figures.

pHFB$_1$_7: ^1H NMR (500 MHz, MeOH-d_4; Fig. S2: the ~30 % HFB_1 content is not annotated) δ 5.09 (dt, J = 11.0, 5.8 Hz, 1H), 3.90–3.85 (m, 1H), 3.75 (ddd, J = 9.5, 6.6, 3.1 Hz, 1H), 3.66–3.61 (m, 2H), 3.42 (dd, J = 8.0, 3.6 Hz, 1H), 3.18–3.13 (m, 1H), 3.12–3.07 (m, 1H), 2.72–2.64 (m, 2H), 2.55 (dd, J = 16.3, 5.7 Hz, 1H), 2.37 (dd, J = 15.7, 7.1 Hz, 1H), 1.88–1.80 (m, 1H), 1.79–1.65 (m, 2H), 1.63–1.47 (m, 1H), 1.47–1.30 (m, 11H), 1.29–1.27 (m, 4H), 1.26–1.04 (m, 4H), 0.97 (d, J = 6.7 Hz, 3H), 0.92 (t, J = 6.5 Hz, 2H), 0.91 (d, J = 6.9 Hz, 7H).

FB$_1$: ^1H NMR (500 MHz, MeOH-d_4; Fig. S6) δ 5.18 (dt, J = 10.8, 3.2 Hz, 1H), 4.97 (dd, J = 8.2, 3.7 Hz, 1H), 3.86 (d, J = 4.3 Hz, 0H), 3.76 (ddd, J = 7.2, 7.2, 4.0 Hz, 1H), 3.68–3.62 (m, 0H), 3.23–3.12 (m, 4H), 2.86–2.59 (m, 6H), 2.58–2.43 (m, 3H), 1.90–1.78 (m, 1H), 1.77–1.66 (m, 2H), 1.60–1.55 (m, 2H), 1.55–1.39 (m, 13H), 1.39–1.32 (m, 1H), 1.30 (d, J = 6.7 Hz, 4H), 1.27–1.06 (m, 2H), 0.99 (d, J = 6.7 Hz, 3H), 0.96 (d, J = 6.8 Hz, 4H), 0.92 (t, J = 6.9 Hz, 4H). ^1H NMR spectrum and assignment for FB_1 agree with the published data (Månsson et al., 2010; Pereira et al., 2009).

HFB$_1$: ^1H NMR (500 MHz, MeOH-d_4; Fig. S8) δ 3.88–3.80 (m, 1H), 3.72–3.63 (m, 3H), 3.25–3.20 (m, 1H), 3.03–2.93 (m, 1H), 2.03–1.93 (m, 1H), 1.76–1.57 (m, 4H), 1.56–1.23 (m, 12H), 1.21 (d, J = 6.5 Hz, 3H), 1.19–1.05 (m, 3H), 1.00 (d, J = 6.7 Hz, 3H), 0.94 (d, J = 7.3 Hz, 3H), 0.93 (d, J = 7.0 Hz, 3H). ^1H NMR for HFB_1 agrees with the published data (Pereira et al., 2009).

2.8. Kinetics of FE1 and FE2 with FB_1 and $pHFB_1$

All substrates and enzyme solutions were diluted in Buffer A (50 mM potassium phosphate buffer supplemented with 100 μg mL^{-1} of BSA, at p*H* 6.0) for the enzyme kinetic measurements. The fermentation supernatants containing FE were diluted to a final enzyme concentration of 2.0 μg L^{-1} in the reactions. Solutions of FB_1 and $pHFB_1$ were diluted to five different concentrations in the range between 4.5 and 165 μM in final reaction volumes of 200 μL. The reaction mixtures were incubated at 37 °C in a TDB-120 Dry Block Thermostat (Biosan, Riga, Latvia). Samples (20 μL) were taken from every enzyme reaction, five times at different time points, depending on the substrate, substrate concentration, and enzyme. The samples were mixed immediately with 113 μL of MeOH to terminate the enzymatic reaction. The reactions (performed in triplicates) were analyzed with HPLC-FLD. Linear equations were fitted to the measured points of the product concentration-time function's diagram with linear regression using Microsoft Excel. During the degradation of FB_1, only those measurement points where the amount of HFB_1 was negligible were evaluated for the fitting. The initial reaction rates were defined as the slope of the linear equation in μM min^{-1}. The fitted linear equations were accepted when the R^2 values were at least 0.995.

Kinetic parameters were obtained by non-linear least square fitting of the Michaelis-Menten equation to the initial reaction rates as a function of the substrate concentration using the drm function of the *drc* package (Ritz et al., 2015) in R (R Core Team, 2021). The quality of the fit was assessed by the *p* values given by the drm package, and by computing the R^2 of the fit using the modelr package of R (Wickham, 2023) (Table S1).

2.9. Non-enzymatic acyl migration kinetics of the partially hydrolyzed FB_1 monoesters

The kinetics of the acyl migration reaction was investigated in the following media: DMSO; MeOH; H_2O; MeOH:H_2O 75:25; Simulated Gastric Fluid (SGF, containing 3.45 mM KCl, 0.45 mM KH_2PO_4, 12.5 mM $NaHCO_3$, 23.6 mM NaCl, 0.05 mM $MgCl_2$, 0.25 mM $(NH_4)_2CO_3$, and 0.075 mM $CaCl_2$, at p*H* 3.0); and Simulated Intestinal Fluid (SIF, containing 3.4 mM KCl, 0.4 mM KH_2PO_4, 42.5 mM $NaHCO_3$, 19.2 mM NaCl, 0.17 mM $MgCl_2$, and 0.3 mM $CaCl_2$, at p*H* 8.5)(Minekus et al., 2014). All solvents were HPLC-grade. Test solutions of $pHFB_1$_7 containing 5 % of $pHFB_1$_6 at a final concentration of 9.0 μM were prepared in the aforementioned media (1 mL). The test solutions in H_2O, DMSO, MeOH, and MeOH:H_2O 75:25 were incubated at 20 °C, and further ones dissolved in H_2O, SGF, and SIF were incubated at 37 °C in the thermostatted sample holder of the HPLC autosampler for 16 h. Each test solution was analyzed five times at equal intervals and immediately analyzed with HPLC-FLD as described above. The measurements were performed in triplicate.

2.10. Calculation of the half-life of $pHFB_1$_7

In the following equations (Eqs. 1–6), [$pHFB_1$_6] and [$pHFB_1$_7] are the concentrations of $pHFB_1$_6 and $pHFB_1$_7, respectively, and k_1 and k_2 are the respective forward and reverse rate constants. The reaction equilibrium is described by Eq. 1:

$$pHFB_1\_7 \underset{k_2}{\overset{k_1}{\rightleftarrows}} pHFB_1\_6 \tag{1}$$

The rate law is defined by Eq. 2:

$$\frac{d[pHFB_1\_7]}{dt} = -k_1 \times [pHFB_1\_7] + k_2 \times [pHFB_1\_6] \tag{2}$$

Direct substitution of $pHFB_1$ species for diacylglycerols in the prior derivation (Laszlo et al., 2008) gave an explicit expression of [$pHFB_1$_7] as a function of time (Eq. 3):

$$[pHFB_1\_7]_t = \frac{[pHFB_1\_7]_0 - [pHFB_1\_7]_e}{e^{C \times k_1 \times t}} + [pHFB_1\_7]_e \tag{3}$$

in which [$pHFB_1$_7]$_0$ and [$pHFB_1$_7]$_e$ are the initial and equilibrium $pHFB_1$_7 concentrations, respectively. The term $C \times k_1$ is related to the equilibrium constant as shown in Eq. 4:

$$C \times k_1 = k_1 + k_2 = \frac{K+1}{K} k_1 \tag{4}$$

in which K is the equilibrium constant, calculated by Eq. 5:

$$K = \frac{k_1}{k_2} = \frac{[pHFB_1\_6]_e}{[pHFB_1\_7]_e}. \quad (5)$$

The $[pHFB_1\_7]_t$ data (data not shown) were fitted to Eq. 3. The sum of the square of the difference between the measured and calculated $[pHFB_1\_7]_t$ values was minimized using Microsoft Excel's Solver, by changing the value of $C \times k_1$. In this experiment, $[pHFB_1\_7]_0$, $[pHFB_1\_6]_e$, and $[pHFB_1\_7]_e$ were measured to be 8.55 μM, 3.87 μM, and 5.13 μM, respectively, therefore K was calculated by Eq. 5 to be 0.754. The rate constants k_1 and k_2 were calculated using Eq. 4. The half-lives of $pHFB_1\_7$ ($t_{1/2}(pHFB_1\_7)$) under different conditions were calculated as shown by Eq. 6:

$$t_{1/2} = \frac{ln(2)}{k_1 + k_2} = \frac{ln(2)}{C \times k_1} \quad (6)$$

2.11. Thermofluor assays of FE1 and FE2

The Thermofluor assays of FE1 and FE2 were performed using the CFX Opus 96 Real-Time PCR System (Bio-Rad Laboratories, Hercules, CA, USA), as described in the manufacturer's protocol (BIO-RAD, 2022). Solutions of FE1 and FE2 were concentrated with a 10 kDa cutoff Amicon Ultra-15 Centrifugal Filter (Merck KGaA) to approximately 6 mg mL^{-1} protein concentration. Measurements were performed in triplicates, in 50 mM potassium phosphate buffer at p*H* 6, at a protein concentration of 0.75 mg mL^{-1}, and ligand concentrations of 100 μM. Melt curves were measured by heating the samples from 25 °C to 95 °C in increments of 0.5 °C, incubating the samples for 5 s at each step. SYPRO Orange Protein Stain 5000× (Thermo Fisher Scientific; Waltham, MA, USA) was used at a final dilution of 5× to detect protein unfolding, which generates a signal on the FRET channel. The T_m values were calculated from the negative derivative of the melting curve, by the software of the RT-PCR System.

2.12. Hydrolysis of FB_1 by FE2 during corn wet-milling at laboratory scale

Corn wet-milling was simulated similarly as described previously by Eckhoff et al. (1996). Briefly, 10 g of whole corn kernel, containing FB_1 (20 ppm, 28 μM), was steeped in distilled water (10 mL) containing sulfur dioxide (2000 ppm) and lactic acid (0.5 *w*/w%). The p*H* of the mixture was adjusted to 4.1, a typical p*H* during industrial corn steeping (Jackson & Shandera, 1995). Four samples were steeped without agitation in a 50 °C water bath for 24 h. FE2 (65 μg) was added to three of the samples, one served as a negative control. After 24 h, the mixtures were filtered through a filter paper. The supernatants and solid residues were processed using the published method (Sydenham, Thiel, et al., 1995), except using Isolute C18 SPE column (Biotage, Uppsala, Sweden). The purified compounds were analyzed by HPLC according to section 2.4.

2.13. Purification of recombinant FE2 for crystallization

Fermentation media containing FE2 was centrifuged, the supernatant was then sterile filtered with 0.22 μm filter, concentrated 80-fold with 10 kDa MWCO Amicon Ultra-15 Centrifugal Filter (Millipore), and dialyzed against 20 mM TRIS, pH 7.5 buffer. Concentrated samples were sterile filtered and centrifuged again before chromatographic purification on a 5-mL HiTrap heparin HP column (GE Healthcare Life Sciences). After equilibrating the column with 10 column volumes of binding buffer (20 mM TRIS, pH 7.5), the supernatant was loaded onto it. The column was washed with 5 column volumes of wash buffer (20 mM TRIS, pH 7.5), proteins were eluted using a linear NaCl gradient, from 0 mM NaCl, 20 mM TRIS pH 7.5 to 1 M NaCl, 20 mM TRIS pH 7.5 over 10 column volumes with a flow rate of 2 mL min^{-1}. Elution was followed by absorbance at 280 nm. Fractions were sampled on SDS-PAGE, and fractions containing FE2 were pooled and further purified with size exclusion chromatography on Superdex 200 Increase 10/300 (GE Healthcare Life Sciences) with 20 mM TRIS pH 7.5. Fractions containing FE2 were pooled and concentrated with AmiconUltra-0.5 10 K centrifugal filter device (Merck Millipore) to a final concentration of 15 mg mL^{-1}. The concentrated protein stock was stored at 4 °C until used for crystallization.

2.14. Crystallization of FE2 and X-ray data collection

A crystal of FE2 was grown in a one-to-one mixture of the protein solution (15 mg mL^{-1}) and the precipitant (0.1 M KCl, 15 *w/v* % PEG 6000, HEPES 0.1 M pH 7.5), using sitting drop vapor diffusion method with 800 nL drops. The crystal appeared in 3 weeks at room temperature. Oil was added as a cryo-protectant to the crystal before plunge-freezing it in liquid nitrogen. X-ray diffraction data were collected at 100 K at Diamond Light Source I03 beamline, with Unattended Data Collection (UDC) mode at a wavelength of 0.97628 Å.

2.15. Structure determination and refinement

Collected data were auto-processed by the AutoProc pipeline (Vonrhein et al., 2011) implemented at the IO3 beamline. The resolution limit cut-off was determined based on the mean intensity correlation coefficient of half-data sets, CC1/2. The structure was solved by molecular replacement using PHASER (McCoy et al., 2007). The initial search model for FE2 was generated using Colab Alphafold2 (Mirdita et al., 2022). Structure refinement of FE2 was performed using the PHENIX (version 1.20.1–4487) with automatic weighting options (Liebschner et al., 2019). Manual model building was done in COOT (Emsley & Cowtan, 2004). Data collection and refinement statistics are summarized in Table S2.

2.16. Docking of fumonisins to the structure of FE2

Initial conformations of FB_1 for docking into FE2: The two initial conformations of fumonisin B_1 with correct stereochemistry, and with a protonated amine group, and deprotonated carbonyl groups (eFB_1 and uFB_1 in Fig. S14), were generated in HyperChem (HyperChem, 2009). The extended chain version of fumonisin B_1 (eFB_1) was obtained from the manually generated zig-zag chain conformation after optimization with Polak-Ribiere conjugate-gradient, for1500 cycles, using the Amber99 force-field (Showalter & Brüschweiler, 2007). The U-shape main-chain conformation of FB_1 (uFB_1) for docking was generated from the eFB_1 structure by molecular dynamics (3 ps, in vacuum, 320 K) followed by optimization with Polack-Ribiere conjugate-gradient, for 1500 cycles using the Amber99 force-field.

Initial conformations of further fumonisins for docking into FE2: The U-shape main-chain conformation of FB_1 (uFB_1) was manually modified (by proper deletions and additions) to generate $pHFB_1\_6$, $pHFB_1\_7$, FB_2, FB_3, FB_4, FA_1, FC_1, and FP_1 structures for docking. The generated structures were refined by optimization with Polack-Ribiere conjugate-gradient, for 1500 cycles, using the Amber99 force-field.

Preliminary docking of FB_1 into the experimental structure of FE2 (PDB ID: 8S6D): A preliminary docking was performed in water-free FE2 structure. The waters were removed from the structure of FE2 (PDB ID: 8S6D), the protein was protonated by OpenBabel (O'Boyle et al., 2011) according to pH 6 in Avogadro^2 (Hanwell et al., 2012), and the HE2 proton from NE2 atom of H427, and the waters were removed in PyMOL. The docking was performed with two initial conformations of FB_1 (eFB_1 and uFB_1, see Fig. S14) using Autodock VINA (Eberhardt et al., 2021; Trott & Olson, 2010) by the DockingPie plugin (Rosignoli & Paiardini, 2022) in PyMOL (DeLano, 2002). The receptor and ligand structures for docking in the DockingPie plugin were imported from PyMOL (prepared FE2 as such, eFB_1 or uFB_1: all torsions are active). The grid settings were imported from the FE2 structure in PyMOL and set in a

way to incorporate all parts of the FE2 structure (centered at X = 28.7, Y = 26.3, Z = 23.6 Å near to S227; grid: 4, dimensions X = 12, Y = 15, Z = 16). With these settings, 5 runs were started (energy range: 3 kcal/mol, exhaustiveness: 8, 50 poses for each). Docking poses were considered as reactive arrangements only when the carbonyl *C*-atom of FB_1 C6-TCA ester was in close vicinity of the *O*-atom of S227 (<4.0 Å) and the carbonyl *O*-atom oriented towards the oxyanion hole. The C19 amino moiety-bearing portion of the FB_1's main chain could fit in the Tyr-hole of FE2 in several docking hits but neither of such docking poses included any ester carbonyls of TCA moieties of FB_1 in reactive distance to S227.

Docking of fumonisin B_1 and the further fumonisins into the R303 corrected experimental structure of FE2 ($FE2_{R303}$): The best-scoring FB_1 arrangement in the preliminary uFB_1 docking set had clash only with two experimental waters (HOH 628 from the oxyanion hole and HOH 744 overlapping with a carboxylate of the TCA ester at C7). Thus, the final docking of the initial uFB_1 conformation was performed into a structure of FE2 with all but these two waters and with a full R303 sidechain ($FE2_{R303}$, created by mutating the virtual A303—being present in the FE2 structure (PDB ID: 8S6D) due to omitting atoms of R303 without sufficient electron densities—to rotamer 1 of R303 using PyMOL (DeLano, 2002)). Docking was performed analogously as described in the preceding section on preliminary docking (energy range: 3 kcal/mol, exhaustiveness: 8, 20 poses for each run). Filtering the docking poses generated with uFB_1 in $FE2_{R303}$ by Autodock VINA (Eberhardt et al., 2021; Trott & Olson, 2010) resulted in a reactive pose with good agreement to the one found in the preliminary set. Dockings of the other fumonisins in this study were performed analogously.

2.17. Refinement of the possible reactive arrangements of fumonisins and tetrahedral intermediates from them within the active site of FE2

The best-scored reactive docking poses for the investigated fumonisins (FB_1, $pHFB_1\_6$, $pHFB_1\_7$, FB_2, FB_3, FB_4, FA_1, FC_1, or FP_1) were energy minimized in the ligand containing $FE2_{R303}$ structure by Amber99 forcefield (Showalter & Brüschweiler, 2007) using HyperChem (HyperChem, 2009). After importing the FE2 structure with the docked pose of the corresponding fumonisin, the bonds and atom types of the fumonisin ligand were checked/corrected (C═O bond for carbonyl, resonance bonds for the carboxylates). The S227 *O*-atom was deprotonated, and the charge of this O-atom was set to −0.65, while H435 remained protonated. The residues around a 15 Å sphere centered at the C10 carbon of the actual fumonisin ligand were set as active site residues (typically 81–92 residues, including the fumonisin ligand) while the other residues of the system were kept frozen, and optimization was performed (Amber99, Polak-Ribier conjugate gradient with 0.1 conversion limit, typically 600 cycles) resulting in the energy minimized structure of the actual fumonisin ligand arrangement within FE2.

The initial tetrahedral intermediate states were generated from the energy-minimized structures of FE2 with the actual fumonisin. Using HyperChem (HyperChem, 2009), the bond between the carbonyl *C*-atom of the reactive TCA ester moiety of the FB_1 ligand and the S227 *O*-atom was created, the bond order of the TCA ester carbonyl C═O was decreased to 1 and the charge of its *O*-atom was set to −0.65, while the charge of the S227 *O*-atom was removed. The same residues around the 15 Å sphere centered at the C10 carbon of the fumonisin ligand were set as active site residues (typically 81–92 residues, including the THI state forming from the fumonisin ligand) while the other residues of the system were kept frozen, and optimization was performed (Amber99, Polak-Ribier conjugate gradient with 0.1 conversion limit, typically 600 cycles) resulting in energy minimized structures of the possible THI-state from the actual fumonisin.

3. Results

3.1. FEs perform regioselective sequential hydrolysis of FB_1

To shed light on the two consecutive steps of FB_1 enzymatic hydrolysis by FEs, we performed FB_1 hydrolysis assays using FE1 or FE2 at 37 °C and analyzed partially hydrolyzed intermediates from the enzymatic reaction. Upon terminating the enzymatic hydrolysis of FB_1 by methanol addition, only one of the two possible $pHFB_1$ was observed in >99 % purity on the HPLC chromatograms (Fig. S1). We isolated the formed $pHFB_1$ regioisomer by preparative HPLC in sufficient quantity for ^{1}H NMR analysis. The ^{1}H NMR spectrum showed a *ddd* signal at 5.11 ppm (J = 10.5, 3.2, 2.1 Hz) (Fig. 2a, Fig. S2), which could be assigned to the C7 proton (Fig. 1) identifying the isolated $pHFB_1$ regioisomer as the $pHFB_1\_7$ monoester.

After incubation of the $pHFB_1\_7$ sample for two weeks at 25 °C, a new peak was visible on the HPLC trace of the sample (Fig. S3), and a new *dd* signal at 4.76 ppm (J = 6.8, 4.7 Hz) appeared on the ^{1}H NMR spectrum (Fig. S4). This new signal can be attributed to the formation of the other regioisomer monoester $pHFB_1\_6$ by a slow spontaneous acyl migration reaction (Wang et al., 2022). The same peak was observed by HPLC analysis when the enzymatic reaction was stopped by boiling for 5 min (Fig. S10).

To assess conditions influencing the kinetics of the acyl migration reaction, the half-life of the $pHFB_1\_7$ monoester was determined in various solvents at room temperature (20 °C) or body temperature (37 °C). Elevated temperature accelerated the acyl migration reaction; a rise of the incubation temperature by 17 °C resulted in an 8-fold decrease in the half-life of $pHFB_1\_7$ in water (Table S3). The half-life of $pHFB_1\_7$ lengthened with increasing solvent polarity in the series of DMSO, MeOH, and water (Table S3), in accordance with an unfavorable effect of high solvent polarity to transition state charge dispersion where the polarity was quantified by the empirical parameter of solvent polarity value (E_T^N) (Reichardt & Welton, 2010). Alkaline conditions mimicking the intestinal fluid (pH 8.5) significantly shortened the half-life of $pHFB_1\_7$, compared to water or strongly acidic conditions mimicking gastric fluid (pH 3) (Table S3). The results can be rationalized by assuming regular ionic mechanisms of acyl migration of the pHFB1s involving the formation of five-member intramolecular ring intermediates in either acid-catalyzed or base-catalyzed way (Fig. S11).

3.2. Enzyme kinetic analysis of FE1 and FE2

To evaluate the kinetics of the two steps of the enzymatic hydrolysis of FB_1, the initial reaction rates (V_0) were measured at different pure FB_1 or pure $pHFB_1\_7$ substrate concentrations, in triplicates. With FB_1 as substrate, the catalytic efficiencies (k_{cat}/K_M) of the two FEs, FE1 and FE2 were similar (Table 1). The turnover number (k_{cat}) of FE1 was higher than that of FE2, while FE2 had a slightly lower K_M value, likely reflecting a greater affinity towards FB_1. A larger difference between the two FEs occurred with $pHFB_1\_7$ as substrate; although the k_{cat} values of FE1 and FE2 were comparable, FE2 had a nearly 10-fold lower K_M value, yielding an order of magnitude difference between catalytic efficiencies of the two enzymes (Table 1).

3.3. FE1 and FE2 display promiscuity in degrading both $pHFB_1\_6$ and $pHFB_1\_7$ fumonisin monoesters

To investigate the ability of FEs to degrade $pHFB_1\_6$, the equilibrium mixture of the two monoesters at substrate saturation concentration was additionally treated with either FE1 or FE2. Should the FE only degrade $pHFB_1\_7$ and not $pHFB_1\_6$, then the rate of formation of HFB_1 would be lower, and a buildup of $pHFB_1\_6$ would occur. Conversely, should the FE degrade both regioisomers at comparable rates, then the decrease in the monoesters would be simultaneous, and the rate of increase in HFB_1 would be comparable to the one measured for the pure $pHFB_1\_7$

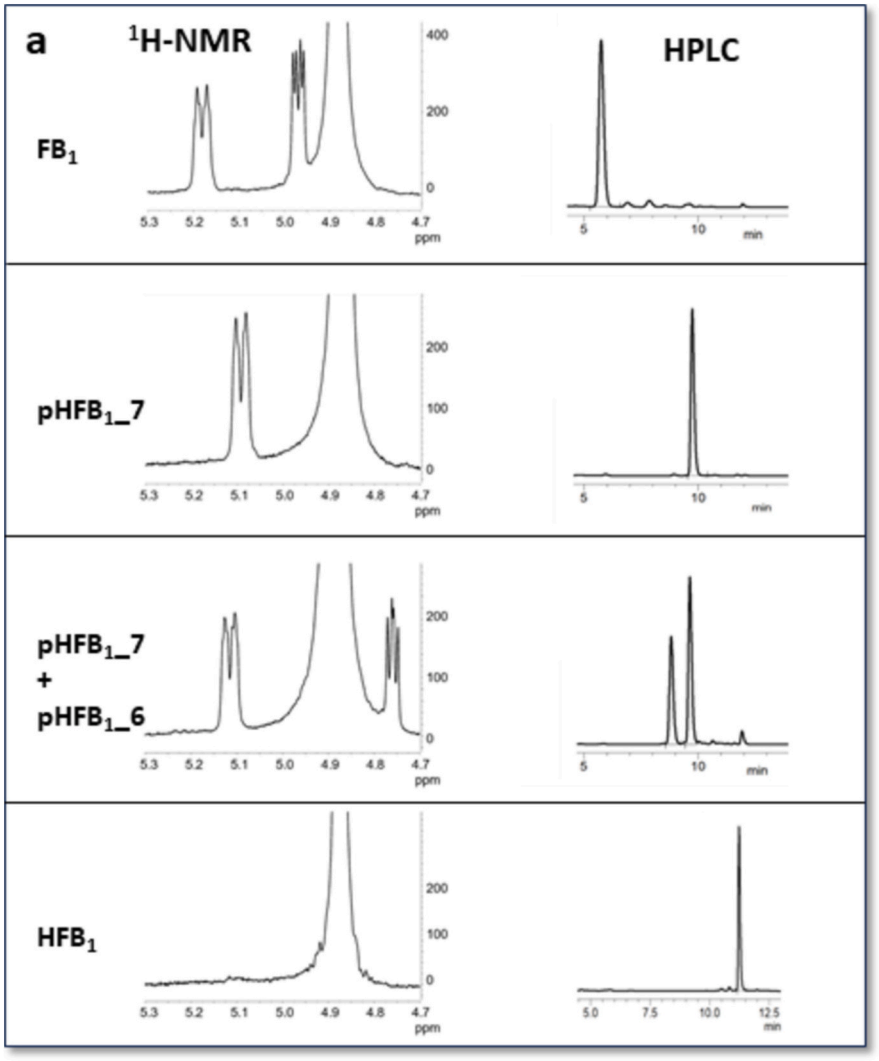

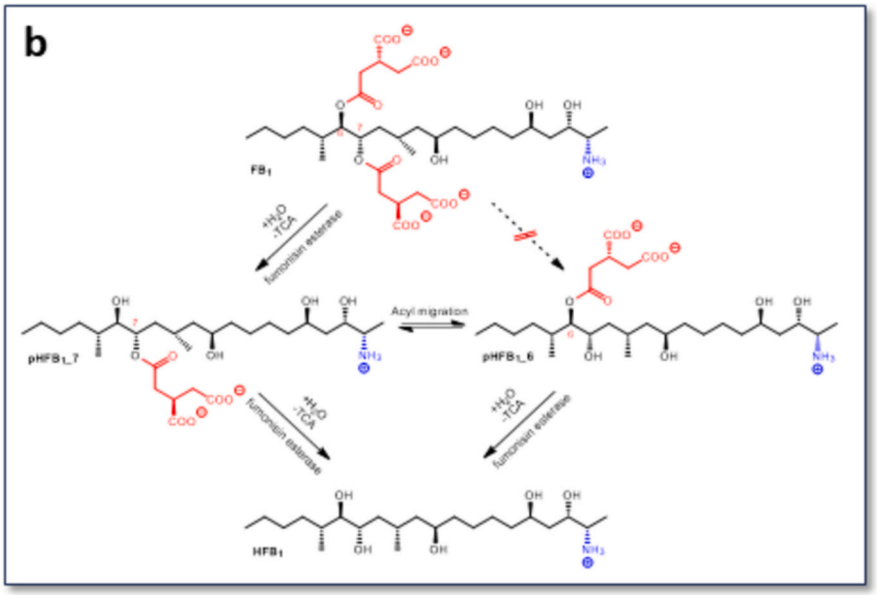

(caption on next page)

Fig. 2. Experimental evidence reveals regioselective sequential hydrolysis of FB_1 by fumonisin B_1 esterases (FEs). (a) Partial ^{1}H NMR spectra and HPLC chromatograms of FB_1 and its metabolites. HPLC trace shows the purity of each compound, while the specific ^{1}H NMR signals between 5.3 and 4.7 identify the chemical substitutions of the C6 and C7 atoms. (b) FE1 and FE2 selectively hydrolyze the TCA ester at the C6 position to produce $pHFB_1$_7. This intermediate can undergo non-enzymatic acyl migration, resulting in the formation of $pHFB_1$_6. Then, FE-s cleave the residual TCA ester from either $pHFB_1$s in a second step to yield the final HFB_1 product of the enzymatic hydrolysis. FE can degrade either $pHFB_1$_6 or $pHFB_1$_7. The complete chromatograms and ^{1}H NMR spectra are included in Figs. S1-S10.

Table 1
Enzyme kinetic parameters of FE1 and FE2 at pH 6.0 and 37 °C.[a]

FE	Substrate	K_M (μM)	k_{cat} (s^{-1})	k_{cat}/K_M (s^{-1} M^{-1})
FE1	FB_1	8.37 ± 0.55	140 ± 2	1.67×10^7
FE1	$pHFB_1$_7	44.3 ± 2.23	121 ± 2	2.73×10^6
FE2	FB_1	6.03 ± 0.41	115 ± 2	1.91×10^7
FE2	$pHFB_1$_7	4.76 ± 0.61	124 ± 3	2.60×10^7

[a] The enzyme kinetic constants have been deposited in the STRENDA database, with access codes; GDLSFH and, EOV8MZ. Data for enzyme kinetics analysis are archived at Mendeley data (Incze, 2024).

substrate. In the reactions of both FE1 and FE2, the concentration of the monoesters decreased simultaneously, and HFB_1 formed at comparable rates to the pure $pHFB_1$_7 reaction (Fig. S12). Therefore, FE1 and FE2 can catalyze the hydrolysis of both $pHFB_1$_7 and $pHFB_1$_6 to HFB_1 with similar efficiencies. Interestingly, while with FE1 both $pHFB_1$ monoesters decreased at comparable rates, with FE2 $pHFB_1$_7 decreased 45 % faster than $pHFB_1$_6.

3.4. Thermal stability of FE1 and FE2

Next, we elucidated the thermostability of FE1 and FE2 at pH 6 by differential scanning fluorimetry. FE2 had a higher temperature of half denaturation (T_m) (55.5 °C) than that of FE1 (51.0 °C), indicating a higher thermal stability of the former (Table S4). TCA and HFB_1 hydrolysis products at 100 μM concentration did not significantly influence the T_m of FE1 or FE2. Both FE1 and FE2 exhibited higher thermal stability than the previously reported FE4 under similar conditions (46.8 °C) (Li et al., 2021).

3.5. FE2 can hydrolyze FB_1 in a simulated corn wet-milling procedure

To investigate the practical applicability of FEs during corn wet-milling, FE2 was tested in the corn steeping step of a simulated corn wet-milling procedure. Under the conventional industrial conditions of 50 °C, p*H* 4.1 and 2000 ppm of SO_2, 6.5 μg of FE2 per 1 g of corn (containing 20 ppm of FB_1 (28 μM)) could hydrolyze 96.3 ± 0.4 % and 95.5 ± 0.8 % of the FB_1 (at 50 °C after 24 h) in the corn steep liquid and in the solid residues of corn, respectively, compared to the control sample without FE2 (Table S5).

3.6. The crystal structure of FE2 reveals its α/β-hydrolase fold and an unusual positively charged substrate binding cavity

To explore the structural basis of FE enzyme specificity, high-throughput crystallization trials were set up with FE2 purified to >99 % homogeneity (see Section 2.13 for details). The crystal structure of FE2 was determined to a maximum resolution of 2.24 Å (Fig. 3, Table S2), and deposited in the PDB under the entry number 8S6D.

The FE2 crystal asymmetric unit contains a single monomer. FE2 exhibits an α/β three-layered sandwich fold typical for α/β-hydrolases (Fig. 3a). The folded β-sheet, composed of 10 β strands (β4-β13), comprises the core of the protein structure surrounded by α-helices and loops interspersed among the β-strands in the primary protein sequence. The fold of FE2 is stabilized by disulfide bridges C97-C116 and C377-C522, which lock the α4-β5 region and the protein *C*-terminus to the α11 helix. FE2 is a serine hydrolase, and its hallmark catalytic triad encompassing S227, E343, and H435 residues is located at the center of the active site. S227 is the nucleophile residue located within hydrogen-bond distance to H435, which is stabilized by the acid E343 (Fig. 3b). Residues G141, G142, and A228 form the oxyanion hole, where a water molecule is coordinated in the structure. The active site of FE2 has an elongated shape with two deep pockets extending from the catalytic center (Fig. 3b). The arginine pocket is lined by three arginines; R258, R300, and R306, which provide a prominent positive electrostatic charge (Fig. 3c). The tyrosine pocket is located at the opposite end of the active site, lined by two tyrosines; Y152 and Y153. Flexible loops of F347-P356, R291-S299, and F446-D456 restrict the border of the active site and define its closed state, limiting solvent access and suggesting some structural rearrangement upon ligand binding (Fig. 3d). Further difference electron densities are present in the active site cavity (Fig. S13), however, no corresponding ligand could be unambiguously identified.

3.7. In silico modeling reveals catalytically relevant substrate binding poses in the FE2 active site

Next, molecular docking to the FE2 structure was performed with AutoDock VINA (Eberhardt et al., 2021; Trott & Olson, 2010). A preliminary docking study using two initial conformations of FB_1—the eFB_1conformation with an extended zig-zag main-chain and the uFB_1 conformation with a U-shape main-chain arrangement (Fig. S14)—indicated no catalytically relevant binding pose within the eFB_1 docking set, while the uFB_1 docking set revealed possible reactive poses. These results demonstrated the U-shape main-chain arrangement to be a more suitable starting conformation for docking, thus this conformation was used in all subsequent modeling. Docking of uFB_1 revealed a pose (FB_1-reactive) as a likely reactive arrangement of FB_1 (Fig. 4a).

In this FB_1-reactive arrangement, the distance between the *C*-atom of the C6 TCA-ester carbonyl and the *O*-atom of S227 is 3.4 Å, and the carbonyl *O*-atom orients towards the oxyanion hole (Fig. 4a). The carboxylates of FB_1 occupy the positively charged arginine pocket, while the tyrosine pocket remains unoccupied (Fig. 4b). The C8-C20 part of the main chain occupies a deep cavity between the most mobile α8-α9 and η6-α10 loops, while the hydrophobic C1-C5 part of the main chain lies in a shorter valley in the vicinity of the mobile α14-α15 loop (Fig. 4c). The polar interactions between the C10-OH, C15-OH, C18-OH, and C19-NH_3^+ groups of the main chain and the residues along the wall of the deep valley play important roles in the stabilization of the reactive conformation with the experimentally observed regioselectivity of the FB_1 substrate.

The two carboxylate groups in the TCA show similar binding properties, but they are not equivalent structurally. Therefore, the relative arrangement of the free carboxylates—attached to the 3 and 4 positions within the TCA esters—were ranked according to their distance from the *N*-atom at the C17 position, the closer being listed first (see Fig. S15 for more explanation). Accordingly, the FB_1-reactive docking pose possesses the C6(4,3), C7(4,3) arrangement.

Energy minimization of the active site of the FE2 with the reactive docking pose of FB_1 resulted in the refined reactive arrangement of FB_1 (Fig. 4d). In addition, the possible tetrahedral intermediate state (THI) of FB_1 was also created and optimized (Fig. 4d). A comparison of these structures indicates that the formation of the tetrahedral intermediate coincides with several conformational changes.

In the FB_1-THI state, H435 flips nearly 40° away from S227, stabilized by the H-bond formation between E226 and H435 (2.8 Å). This

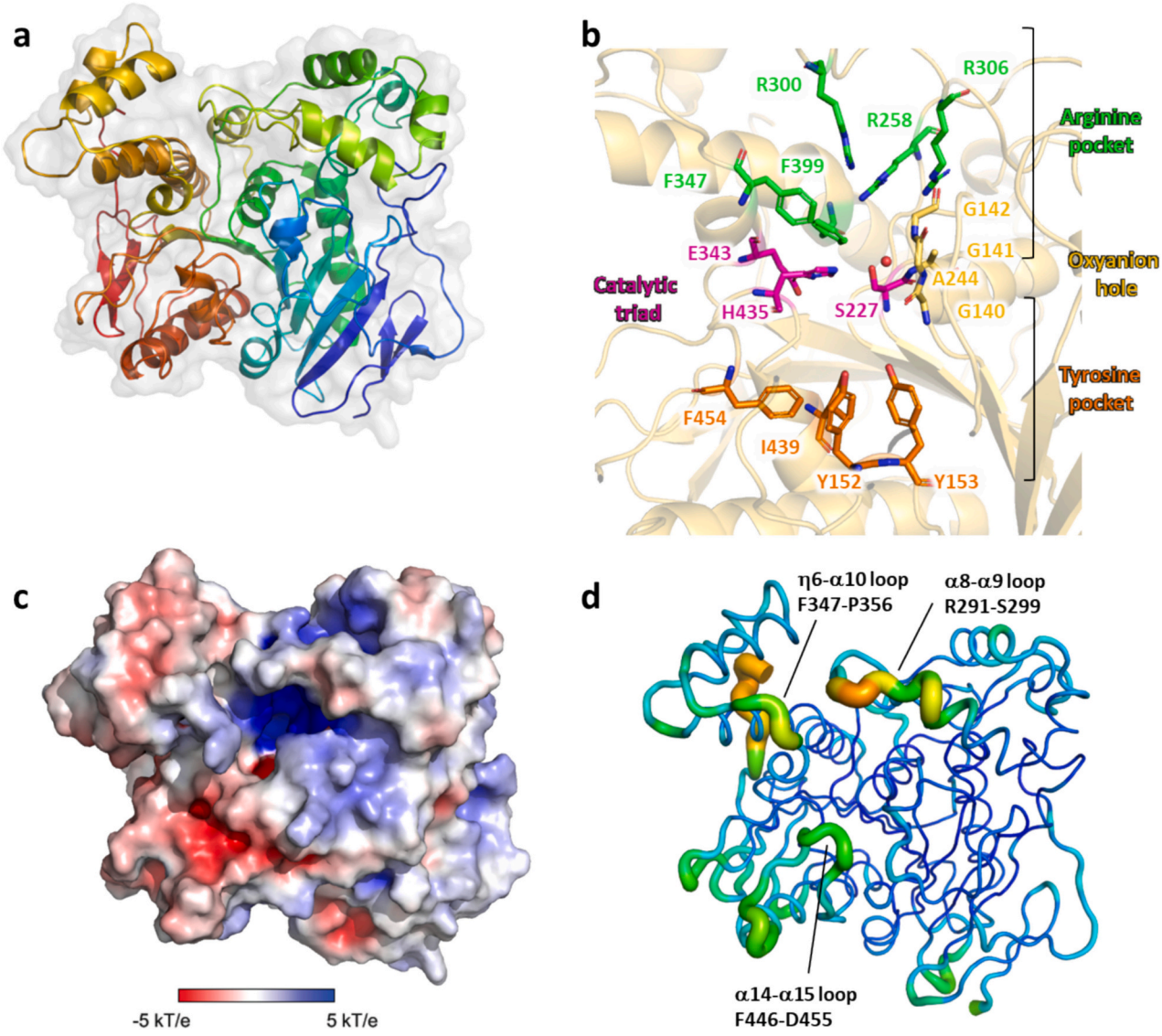

Fig. 3. Crystal structure of FE2 reveals its α/β-hydrolase fold and an unusual positively charged substrate binding cavity. (a) FE2 (PDB: 8S6D) shows a classical α/β hydrolase fold, with 21 α helixes and 13 β sheets. (b) The FE2 active site hosts the catalytic residues; S227, H435 and E343 (pink carbons in stick representation), the oxyanion hole residues (yellow carbons in stick representation), the arginine pocket (green carbons in stick representation) and the tyrosine pocket (orange carbons in stick representation) (c) Electrostatic surface potential representation of the protein active site shows the high positive charge concentration in the arginine pocket. (d) Flexible loops surrounding the active site define a closed state of the FE2 active site in the current structure. (For interpretation of the references to colour in this figure legend, the reader is referred to the web version of this article.)

event allows the hydrophobic C1-C5 part of the main chain to get closer to S227 upon forming the tetrahedral intermediate. The lower energy of the FB_1-THI state, as compared to the energy-minimized FB_1 state (Fig. 5a) indicates a smooth, almost barrier-free transition of FB_1 to the FB_1-THI state. These results suggest a significant catalytic role for E226 in the hydrolytic action of FE2. Worth noting that FE1 contains also glutamic acid residue preceding the catalytic serine.

3.8. *Modeling predicts FE2 to be a general fumonisin esterase*

To evaluate the behavior of the partially hydrolyzed monoesters, the U-shape conformations of the $pHFB_1$_6 and $pHFB_1$_7 were docked to the FE2 structure, similarly to FB_1. The THI states were generated from the best-docking-score reactive arrangements of $pHFB_1$_6 bond formation between $N_{\pi\text{-H435}}$-O_{E226} and $pHFB_1$_7 similarly to the FB_1-THI state. Comparison of the refined $pHFB_1$_6 / $pHFB_1$_6-THI (Fig. S16a) and the $pHFB_1$_7 / $pHFB_1$_7-THI structures (Fig. S16b) indicated a similar movement of E226 and H435 as in case of FB_1, with the nearly 40° flip of H435 and the H-bond formation between E226 and H435 (2.8 Å). The even lower energy values of the energy minimized $pHFB_1$-THI states as compared to the corresponding $pHFB_1$ states (Fig. 5a) indicate an even smoother transition of the regioisomeric $pHFB_1$s into the corresponding $pHFB_1$-THI state as in the case of FB_1.

In silico docking and structural refinement of the best-scored reactive docking arrangements and the corresponding THI states were extended to a representative set of fumonisins (Braun & Wink, 2018; Kamle et al., 2019) (Fig. 5 and Fig. S17). These include FB_2, FB_3, and FB_4, which represent the effects of the OH-substituents at the aminopolyol backbone; FA_1, FC_1, and FP_1, which allow assessment of changes at the *N*-bearing C19-atom of the aminopentol backbone as compared to FB_1. All these fumonisins share the aminopolyol backbone with two TCA monoesters as C6 and C7 substituents. Structural differences include the presence of either OH or H moiety at C16, methyl/H at C19, and acetylated/free amine state of C19-NH_2.

Modeling revealed all these fumonisins to occupy a catalytically competent pose within the FE2 active site cavity (Fig. S17),

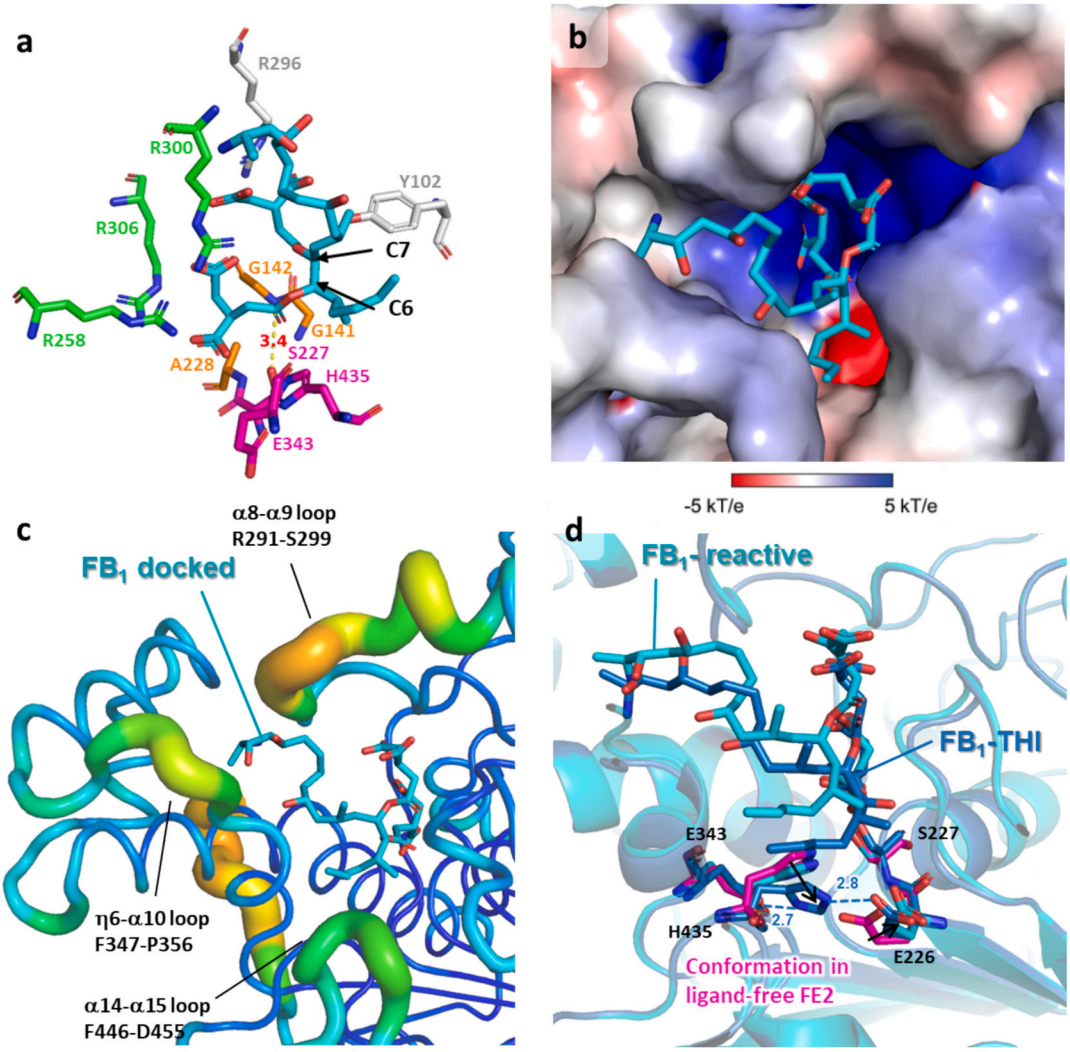

Fig. 4. In silico modeling reveals a catalytically relevant substrate binding pose of FB_1 in the FE2 active site. (a) Arrangement of the best-scored catalytically relevant FB_1 (cyan) docking pose in the active site of FE2. The carbons of catalytic residues are colored in magenta, the oxyanion hole residues in orange, the arginine pocket residues in green, and additional residues in gray. (b) The negatively charged carboxylates of FB_1 bind in the positively charged arginine pocket of the active site. (c) The C8-C20 part of FB_1 binds between the most mobile loops of FE2 (mobility according to B-factors is indicated by tube diameter and coloring of the main chain of FE2: from the least mobile – smallest diameter in blue to the most mobile – largest diameter in orange). (d) Arrangement of the catalytically relevant fumonisin substrate binding poses and the tetrahedral intermediates. The original arrangement of the catalytic residues is shown in magenta; the energy-minimized structure with FB_1 is in cyan, while the energy minimized structure with the tetrahedral intermediate (THI) from it is in blue. (For interpretation of the references to colour in this figure legend, the reader is referred to the web version of this article.)

characterized by a distance of the side-chain *O*-atom of catalytic S227 to the carbonyl moiety of the scissile TCA ester within 4.5 Å. Interactions between the arginine pocket and the leaving TCA moiety carboxylates had a unanimous decisive effect on the orientation of the leaving TCA ester for hydrolysis (Fig. 5). Other structural regions of the docked fumonisins were accommodated within the FE2 active site in heterogeneous orientations. A common feature in all fumonisins was the nearly 40° flip of H435 with H-bond between $N_{\pi\text{-H435}}$-O_{E226} (~2.8 Å) in the fumonisin-THI states (Fig. S17).

Analysis of the docked and refined structures (Fig. 5a and Fig. S17) suggest that relatively small structural alterations may significantly influence the regioselectivity of FE2. The computational results predict that FE2 favors the hydrolysis of the C7 ester of FB_2, FB_3, FB_4, and FC_1. All these fumonisins bound in a C7(4,3) except for FC_1. Only in the case of FP_1, modeling predicts the same C6 regioselectivity as for FB_1, however with the reversed C6(3,4) orientation. Based on the docking scores and the computed energy values, alterations of the OH-substituents at the aminopolyol backbone reduce the affinity of the substrates. Meanwhile changes at the *N*-bearing C19-atom have a more significant effect on binding; the acylated FA_1 appears to be the least preferred substrate for FE2 (Fig. 5a). Collectively, the accommodation of these fumonisins in the FE2 active site in a catalytically relevant orientation, supported by prominent interactions with the arginine pocket indicates FE2 to be a general, rather than a selective fumonisin B_1 esterase.

4. Discussion

4.1. Kinetics and structural analysis explain the biotechnology potential of FE2

Elimination of the presence of mycotoxins in food or feed represents an immediate food industry challenge. Identification of mycotoxin degrading enzymes, followed by their comprehensive enzymatic characterization (Lyagin & Efremenko, 2019) and structure-based enzyme mechanism elucidation (Fruhauf et al., 2024), allow exploiting their full biotechnological potential in the food industry.

Before the detailed kinetics analysis it should be mentioned that possibility of the acyl migration reaction must not be neglected in any

a

Fumonisin	Leaving TCA (-)	Affinity (kcal/mol)	$d_{O\text{-}C\ (dock)}$ (Å)	$d_{O\text{-}C\ (opt.)}$ (Å)	$\Delta E_{S\text{-}THI}$ (kcal/mol)
FB_1	C6(4,3)	-6.508	3.3	3.7	-7
$pHFB_1\_6$	C6(4,3)	-6.238	3.1	4.3	-43
$pHFB_1\_7$	C7(4,3)	-6.532	3.5	3.4	-11
FB_2	C7(4,3)	-6.875	2.8	3.6	13
FB_3	C7(4,3)	-6.917	2.9	4.2	1
FB_4	C7(4,3)	-7.176	2.8	3.3	6
FA_1	C7(4,3)	-6.667	4.3	4.1	38
FC_1	C7(3,4)	-6.905	2.8	3.9	15
FP_1	C6(3,4)	-6.954	3.3	3.2	-18

b

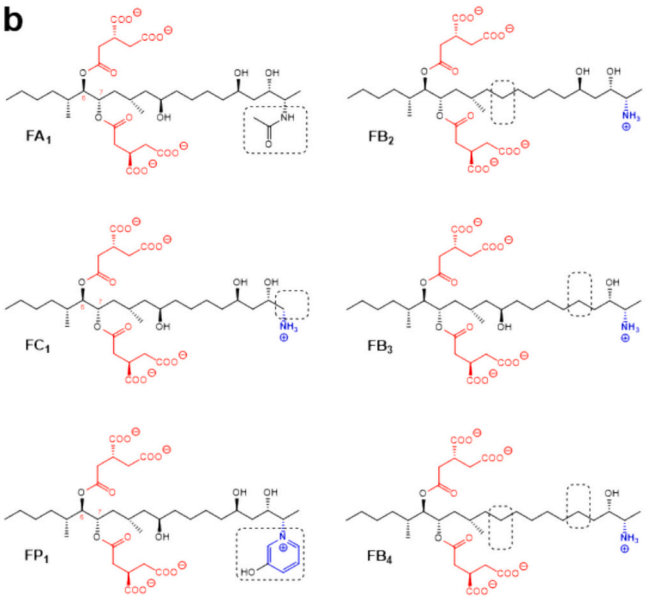

Fig. 5. Modeling predicts FE2 to be a general fumonisin esterase. (a) Details of the docking poses of the fumonisins analyzed by docking; characteristic reactive TCA ester arrangements; docking scores (affinity), O_{S227}-$C_{C=O}$ distances of the docking poses (dock.), and of the energy minimized ligand-binding states (opt.), and the energy difference between the THI and substrate (S) states of several fumonisins and THIs from them. (b) The structures of fumonisins analyzed by docking. The negatively charged moieties are red, the positively charged parts are blue, and the structural differences compared to fumonisin B_1 are marked by the boxes with staggered lines. (For interpretation of the references to colour in this figure legend, the reader is referred to the web version of this article.)

investigation of mycotoxins that contain mono-substituted vicinal diol functional groups, as environmental conditions or sample processing may influence the results of the study (Grenier et al., 2017; Hahn et al., 2015; Heinl et al., 2010; Liu et al., 2022; Masching et al., 2016; Neckermann et al., 2022; Schwartz-Zimmermann et al., 2018).

Our enzyme mechanism investigations of FE1 and FE2 revealed both to be efficient catalysts, with FE2 possessing a higher catalytic efficiency in the complete degradation of FB_1 to HFB_1.

Detailed chemical analyses provided insight into acyl migration that may influence detoxification in biotechnological applications. The turnover number and catalytic efficiency of these FEs exceed those of "average enzymes" (Bar-Even et al., 2011)(10 s^{-1} and 1.25 × 10^5 s^{-1} M^{-1}, respectively) by one order of magnitude and have lower K_M values than ~75 % of them, which make them highly suitable for biotechnological applications. Additionally, the K_M values of FE2 are close to the maximum levels specified by the European Commission (EU Commission Recommendation, 2016) and U.S. Food and Drug Administration (FDA, 2001) for fumonisins in foods (2–4 ppm, which are equal to 2.8–5.5 μM) and feeds (5–100 ppm, which are equal to 6.9–138.5 μM), further ascertaining that FE2 is a promising candidate for the complete hydrolysis of FB_1. FE2—applied at the beginning of the corn refining process in an early soaking step of the wet milling process—showed excellent potential for the hydrolytic degradation of FB_1 contamination. This may provide an opportunity for fumonisin-contaminated grains to be processed, which would otherwise have to be discarded and destroyed.

4.2. Structure-based assessment of the enzyme efficiency of fumonisin hydrolyzing enzymes

Several enzymes have been reported to possess fumonisin hydrolyzing capacity. From the five reported FEs (Duvick et al., 1998; Heinl et al., 2010; Li et al., 2021), the protein sequences of four could be unambiguously identified (Fig. S18). To assess the structure-function relationship of fumonisin hydrolyzing enzymes, their structural models were generated using AlphaFold2 (Mirdita et al., 2022) based on the FE2 crystal structure as a template. Sequence and structure comparison revealed that the serine esterase catalytic triad residues are conserved in FE1–4. (Fig. S18 and S19). Residues forming the oxyanion hole are also conserved except for FE4, where an Ala is in the equivalent position to G142. The herein-identified putative catalytic residue E226 is present in FE1 and FE2, while in FE3 and FE4 a glutamine residue occupies the same position. Structures showed more versatility in the pocket topologies; in FE1 and FE2, both the arginine and the tyrosine pockets are present (Fig. S19), while in FE3 or FE4, none of the two pockets are present, and only Y153 is conserved through all four enzymes (Fig. S19). The absence of the arginine pocket and E226 can explain the large difference in enzyme activity of FE1 and FE2 (69.6 IU mg^{-1} and 70.6 IU mg^{-1}, at 37 °C and 6.5 μM FB_1, respectively) as compared to FE4 (1.12 IU mg^{-1}, at 30 °C and the same substrate concentration, Li et al., 2021). However, the lack of detailed kinetic data for FE3 and FE4 prevents their comprehensive enzymatic assessment.

To explore the closest structural homologs of FE2, its structure was compared against a representative subset of structures of the Protein Data Bank (PDB 50) using the DALI server (Holm et al., 2023). The ten most similar structures were compared to FE2 (Table S6). The catalytic triad, the oxyanion residues, and the E226 (except for one Q) were conserved in the ten closest structural homologs (Fig. S20). The arginine pocket was consistently absent in the homologs; structures showed high diversity in this region. In some, it is open to the surface of the protein, like in the most similar PNB esterase (PDB ID: 1C7J)(Spiller et al., 1999), or the carboxylesterase EST55 (PDB ID: 2OGS)(Liu et al., 2007). Meanwhile, in other enzymes, like the carboxylesterase 2 (PDB ID: 8AXC)(Eisner et al., 2022), the nicotinamide substrate is bound in the corresponding location as the arginine pocket, despite its cavity being formed by hydrophobic residues. Similarly, to the four FEs, Y153 was also conserved in eight of the ten structures. This analysis suggests the arginine pocket to be the critical specific structural feature that confers the high specific activity to fumonisin B_1 of FE1 and FE2, while the tyrosine pocket may be a structural remnant from the general α/β hydrolase fold (Younus et al., 2017).

4.3. Fumonisin esterase FE2 represents a biocatalytic tool for general fumonisin hydrolysis

More than 28 fumonisins have been characterized so far (Rheeder et al., 2002). They all share a common hydrophobic backbone, one amino group on the backbone, and the two TCA groups. Although vast research is available for the prevalence and biological effects of the most common FB_1 (EFSA Panel on Contaminants in the Food Chain et al., 2022), such information is scarce for the other fumonisins, mostly due to the lack of convenient analytical methods. Docking of FE2 with representative fumonisins from FA, FB, FC, and FP classes revealed

catalytically relevant positioning of these mycotoxins within the active site. This is supported by both the prominent positive charge at the arginine pocket, that efficiently oriented the leaving TCA ester for hydrolysis and the flexible, solvent-accessible active site entrance of the enzyme, that allowed accommodation of chemically variable fumonisin moieties without forming conserved ligand binding interactions. These features could potentially allow promiscuity of FEs in binding and hydrolysis of FB_1 and further A, B, C, and P class fumonisin mycotoxins (representative structures are shown in Fig. 5). Further studies are required for a comprehensive characterization of FE2-mediated enzymatic hydrolysis of various class A, B, C, P fumonisin mycotoxins.

5. Conclusions

Fumonisin esterases have several potential applications in agriculture and food safety. They could be used for mycotoxin bioremediation to detoxify fumonisin-contaminated crops, as feed additives to mitigate toxic effects on fumonisins in livestock feed (EFSA Panel on Additives and Products or Substances used in Animal Feed et al., 2024), and during food processing, such as corn refinement, to produce safe and healthy food products.

Our work sheds light on multiple important fumonisin esterase-related features at the molecular level. This study revealed *i)* the high regioselectivity in the first step of the two-step enzymatic hydrolysis of fumonisin B_1 (which was misinterpreted previously in the literature); *ii)* the unambiguous structure assignation of the pure regioisomeric monoester intermediate and the factors influencing its chemical stability; *iii)* the accurate enzyme kinetic parameters of two FEs under a chosen, physiologically relevant condition for fumonisin B_1 and for the isolated pure monoester intermediate; *iv)* the first X-ray structure of a fumonisin esterase and the structure-function relationships of FEs in fumonisin hydrolysis.

Understanding FE structure and its enzymatic mechanism enables rational enzyme design with optimal properties and improves the potential for applying these enzymes to mitigate the impact of fumonisins on human and animal health.

CRediT authorship contribution statement

Dániel J. Incze: Writing – original draft, Investigation, Conceptualization. **Zsófia Molnár:** Investigation. **Gergely N. Nagy:** Writing – review & editing, Validation, Investigation, Conceptualization. **Ibolya Leveles:** Investigation. **Beáta G. Vértessy:** Validation, Resources. **László Poppe:** Writing – review & editing, Supervision, Resources, Investigation, Conceptualization. **Zsófia Bata:** Writing – review & editing, Validation, Resources, Conceptualization.

Declaration of competing interest

The authors declare the following financial interests/personal relationships which may be considered as potential competing interests: Dániel János Incze and Zsófia Bata were employees of Dr. Bata Ltd. during this study.

Acknowledgements

The research reported in this paper is part of project no. TKP2021-EGA-02, implemented with the support provided by the Ministry for Innovation and Technology of Hungary from the National Research, Development and Innovation Fund (NRDIF), financed under the TKP2021 funding scheme. Project no. C1341189 has been implemented with support by the Ministry of Culture and Innovation of Hungary from the National Research, Development and Innovation Fund, financed under the KDP-2021 funding scheme. The research has been supported by Project RRF-2.3.1-21-2022-000 15, which has been implemented with the support provided by the European Union. BGV was also supported by the National Research, Development and Innovation Fund of Hungary (K135231, K146890, NKP-2018-1.2.1-NKP-2018-00005, 2022–1.2.2-TÉT-IPARI-UZ-2022-00003), and the ICGEB Research Grants Programme 2023 (CRP/HUN23–02). GNN was supported by the János Bolyai Research Scholarship of the Hungarian Academy of Sciences.

We thank Viola Horvath (Budapest University of Technology and Economics, Hungary) for the useful discussions about preparative HPLC separation, and Judit Hohmann (University of Szeged, Hungary) for her help in evaluating NMR spectra. The authors would like to thank Diamond Light Source for beamtime (proposal mx34263), and the staff of beamline I03 for assistance with crystal testing and data collection.

Appendix A. Supplementary data

Supplementary data to this article can be found online at https://doi.org/10.1016/j.foodchem.2025.143110.

Data availability

Raw data for the kinetics of FEs are archived at Mendeley Data (Incze, 2024). Further data will be made available upon request to the corresponding authors.

References

ATUM. (2017). Culture and Induction Protocol to Screen for Protein Expression in *Pichia pastoris*. https://www.atum.bio/assets/pdf/Pichia_Culture_and_Induction_Protocol6.pdf (accessed 5 October 2022).

Bar-Even, A., Noor, E., Savir, Y., Liebermeister, W., Davidi, D., Tawfik, D. S., & Milo, R. (2011). The moderately efficient enzyme: Evolutionary and physicochemical trends shaping enzyme parameters. *Biochemistry, 50*, 4402–4410. https://doi.org/10.1021/bi2002289

BIO-RAD. (2022). Protein Thermal Shift Assays Made Easy with the Bio-Rad Family of CFX Real-Time PCR Systems. https://www.bio-rad.com/webroot/web/pdf/lsr/literature/Bulletin_7180.pdf (accessed 6 May 2023).

Braun, M. S., & Wink, M. (2018). Exposure, occurrence, and chemistry of Fumonisins and their cryptic derivatives. *Comprehensive Reviews in Food Science and Food Safety, 17*, 769–791. https://doi.org/10.1111/1541-4337.12334

Chen, J., Wei, Z., Wang, Y., Long, M., Wu, W., & Kuca, K. (2021). Fumonisin B_1: Mechanisms of toxicity and biological detoxification Progress in animals. *Food Chemistry and Toxicology, 149*, Article 111977. https://doi.org/10.1016/j.fct.2021.111977

DeLano, W. L. (2002). The PyMOL molecular graphics system, 2002. (PyMOL version 2.5.5). https://pymol.org.

Duvick, J., Rood, T., Maddox, J., & Gilliam, J. (1998). Detoxification of mycotoxins in planta as a strategy for improving grain quality and disease resistance: Identification of Fumonisin-degrading microbes from maize. In *molecular genetics of host-specific toxins in plant disease. Developments in plant pathology, Vol. 13. Springer, Dordrecht, 1998*, 369–381. https://doi.org/10.1007/978-94-011-5218-1_41

Eberhardt, J., Santos-Martins, D., Tillack, A. F., & Forli, S. (2021). AutoDock Vina 1.2.0: New docking methods, expanded force field, and Python bindings. *Journal of Chemical Information and Modeling, 61*, 3891–3898. https://doi.org/10.1021/acs.jcim.1c00203

Eckhoff, S. R., Singh, S. K., Zehr, B. E., Rausch, K. D., Fox, E. J., Mistry, A. K., … Keeling, P. L. (1996). A 100-g laboratory corn wet-milling procedure. *Cereal Chemistry, 73*(1), 54–57.

EFSA Panel on Additives and Products or Substances used in Animal Feed, Bampidis, V., Azimonti, G., Bastos, M. L., Christensen, H., Dusemund, B., … Radovnikovic, A. (2024). Safety and efficacy of a feed additive consisting of fumonisin esterase produced with *Komagataella phaffii* NCAIM (P) Y001485 for all pigs (piglets, pigs for fattening, sows and minor growing and reproductive porcine species) (Dr. Bata Ltd.). *EFSA Journal, 22*, Article e8614. https://doi.org/10.2903/j.efsa.2024.8614

EFSA Panel on Contaminants in the Food Chain, Knutsen, H. K., Alexander, J., Barregård, L., Bignami, M., Brüschweiler, B., … Oswald, I. P. (2018). Risks for animal health related to the presence of fumonisins, their modified forms and hidden forms in feed. *EFSA Journal, 16*(5), Article e05242. https://doi.org/10.2903/j.efsa.2018.5242

EFSA Panel on Contaminants in the Food Chain, Schrenk, D., Bignami, M., Bodin, L., Chipman, J. K., del Mazo, J., … Hoogenboom, L. R. (2022). Scientific Opinion on the assessment of information as regards the toxicity of fumonisins for pigs, poultry and horses. *EFSA Journal, 20*, Article e07534. https://doi.org/10.2903/j.efsa.2022.7534

Eisner, H., Riegler-Berket, L., Gamez, C. F. R., Sagmeister, T., Chalhoub, G., Darnhofer, B., … Oberer, M. (2022). The crystal structure of mouse Ces2c, a potential Ortholog of human CES2, shows structural similarities in substrate regulation and product release to human CES1. *International Journal of Molecular Sciences, 23*, 13101. https://doi.org/10.3390/ijms232113101

Emsley, P., & Cowtan, K. (2004). Coot: Model-building tools for molecular graphics. *Acta Crystallographica Section D Biological Crystallography, 60*, 2126–2132. https://doi.org/10.1107/S0907444904019158

Eskola, M., Kos, G., Elliott, C. T., Hajšlová, J., Mayar, S., & Krska, R. (2020). Worldwide contamination of food-crops with mycotoxins: Validity of the widely cited 'FAO estimate' of 25%. *Critical Reviews in Food Science and Nutrition, 60*, 2773–2789. https://doi.org/10.1080/10408398.2019.1658570

EU Commission Recommendation. (2016). 2016/1319 of 29 July 2016 amending Recommendation 2006/576/EC as regards deoxynivalenol, zearalenone and ochratoxin A in pet food (Text with EEA relevance). https://eur-lex.europa.eu/legal-content/EN/TXT/?uri=CELEX:32016H1319.

FDA. (2001). Guidance for Industry: Fumonisin Levels in Human Foods and Animal Feeds. https://www.fda.gov/regulatory-information/search-fda-guidance-documents/guidance-industry-fumonisin-levels-human-foods-and-animal-feeds.

Fruhauf, S., Pühringer, D., Thamhesl, M., Fajtl, P., Kunz-Vekiru, E., Höbartner-Gussl, A., … Moll, W. D. (2024). Bacterial lactonases ZenA with noncanonical structural features hydrolyze the mycotoxin Zearalenone. *ACS Catalysis, 14*, 3392–3410. https://doi.org/10.1021/acscatal.4c00271

Green, M. R., & Sambrook, J. (2018). The Hanahan method for preparation and transformation of competent *Escherichia coli*: High-efficiency transformation. *Cold Spring Harbor Protocols, 2018*(3). https://doi.org/10.1101/pdb.prot101188. pdb.prot101188.

Grenier, B., Bracarense, A.-P. F. L., Schwartz, H. E., Trumel, C., Cossalter, A.-M., Schatzmayr, G., … Oswald, I. P. (2012). The low intestinal and hepatic toxicity of hydrolyzed fumonisin B1 correlates with its inability to alter the metabolism of sphingolipids. *Biochemical Pharmacology, 83*, 1465–1473. https://doi.org/10.1016/j.bcp.2012.02.007

Grenier, B., Schwartz-Zimmermann, H. E., Gruber-Dorninger, C., Dohnal, I., Aleschko, M., Schatzmayr, G., … Applegate, T. J. (2017). Enzymatic hydrolysis of Fumonisins in the gastrointestinal tract of broiler chickens. *Poultry Science, 96*, 4342–4351. https://doi.org/10.3382/ps/pex280

Hahn, I., Nagl, V., Schwartz-Zimmermann, H. E., Varga, E., Schwarz, C., Slavik, V., … Dall'Asta, C., Krska, R., Moll, W.-D., Berthiller, F.. (2015). Effects of orally administered Fumonisin B_1 (FB_1), partially hydrolysed FB_1, hydrolysed FB_1 and *N*-(1-deoxy-D-Fructos-1-yl) FB_1 on the sphingolipid metabolism in rats. *Food and Chemical Toxicology, 76*, 11–18. https://doi.org/10.1016/j.fct.2014.11.020

Hanwell, M. D., Curtis, D. E., Lonie, D. C., Vandermeersch, T., Zurek, E., & Hutchison, G. R. (2012). Avogadro: An advanced semantic chemical editor, visualization, and analysis platform. *Journal of. Cheminformatics, 4*, 17. https://doi.org/10.1186/1758-2946-4-17 (Avogadro2, Version: 1.99.0: https://two.avogadro.cc.

Heinl, S., Hartinger, D., Thamhesl, M., Vekiru, E., Krska, R., Schatzmayr, G., … Grabherr, R. (2010). Degradation of Fumonisin B_1 by the consecutive action of two bacterial enzymes. *Journal of Biotechnology, 145*, 120–129. https://doi.org/10.1016/j.jbiotec.2009.11.004

Holm, L., Laiho, A., Toronen, P., & Salgado, M. (2023). DALI shines a light on remote homologs: One hundred discoveries. *Protein Science, 23*, Article e4519. https://doi.org/10.1002/pro.4519

Humpf, H. U., & Voss, K. A. (2004). Effects of thermal food processing on the chemical structure and toxicity of Fumonisin mycotoxins. *Molecular Nutrition & Food Research, 48*, 255–269. https://doi.org/10.1002/mnfr.200400033

HyperChem. (2009). Version 8.0.8. https://www.hypercubeusa.com.

Incze, D. J. (2024). Kinetic data for fumonisin esterases. *Mendeley Data, V1*. https://doi.org/10.17632/3vmzmb9k6y.1

Incze, D. J., Poppe, L., & Bata, Z. (2023). Optimization workflow of Fumonisin esterase production for biocatalytic degradation of Fumonisin B_1. *Life, 13*(9), 1885. https://doi.org/10.3390/life13091885

Jackson, D. S., & Shandera, D. L. (1995). Corn wet milling: Separation chemistry and technology. *Advances in Food and Nutrition Research, 38*, 271–300. https://doi.org/10.1016/S1043-4526(08)60085-6

Kamle, M., Mahato, D. K., Devi, S., Lee, K. E., Kang, S. G., & Kumar, P. (2019). Fumonisins: Impact on agriculture, food, and human health and their management strategies. *Toxins (Basel)., 11*, 328. https://doi.org/10.3390/toxins11060328

Laszlo, J. A., Compton, D. L., & Vermillion, K. E. (2008). Acyl migration kinetics of vegetable oil 1,2-diacylglycerols. *JAOCS, Journal of the American Oil Chemists' Society, 85*(4), 307–312. https://doi.org/10.1007/s11746-008-1202-5

Lee, H. J., & Ryu, D. (2017). Worldwide occurrence of mycotoxins in cereals and cereal-derived food products: Public health perspectives of their co-occurrence. *Journal of Agricultural and Food Chemistry, 65*, 7034–7051. https://doi.org/10.1021/acs.jafc.6b04847

Li, Z., Wang, Y., Liu, Z., Jin, S., Pan, K., Liu, H., Liu, T., Li, X., Zhang, C., Luo, X., Song, Y., Zhao, J., & Zhang, T. (2021). Biological detoxification of Fumonisin by a novel carboxylesterase from Sphingomonadales bacterium and its biochemical characterization. *International Journal of Biological Macromolecules, 169*, 18–27. https://doi.org/10.1016/j.ijbiomac.2020.12.033

Liebschner, D., Afonine, P. V., Baker, M. L., Bunkoczi, G., Chen, V. B., Croll, T. I., … Adams, P. D. (2019). Macromolecular structure determination using X-rays, neutrons and electrons: Recent developments in Phenix. *Acta Crystallographica Section D Structural Biology, 75*, 861–877. https://doi.org/10.1107/S2059798319011471

Liu, M., Zhao, L., Gong, G., Zhang, L., Shi, L., Dai, J., … Sun, L. (2022). Invited review: Remediation strategies for mycotoxin control in feed. *Journal of Animal Science and Biotechnology, 13*(1), 19. https://doi.org/10.1186/s40104-021-00661-4

Liu, P., Ewis, H. E., Tai, P. C., Lu, C. D., & Weber, I. T. (2007). Crystal structure of the *Geobacillus stearothermophilus* carboxylesterase Est55 and its activation of prodrug CPT-11. *Journal of Molecular Biology, 367*(1), 212–223. https://doi.org/10.1016/j.jmb.2006.12.067

Lyagin, I., & Efremenko, E. (2019). Enzymes for detoxification of various mycotoxins: Origins and mechanisms of catalytic action. *Molecules, 24*, 2362. https://doi.org/10.3390/molecules24132362

Månsson, M., Klejnstrup, M. L., Phipps, R. K., Nielsen, K. F., Frisvad, J. C., Gotfredsen, C. H., & Larsen, T. O. (2010). Isolation and NMR characterization of Fumonisin B_2 and a new Fumonisin B_6 from *aspergillus Niger*. *Journal of Agricultural and Food Chemistry, 58*, 949–953. https://doi.org/10.1021/jf902834g

Masching, S., Naehrer, K., Schwartz-Zimmermann, H.-E., Sărăndan, M., Schaumberger, S., Dohnal, I., Nagl, V., & Schatzmayr, D. (2016). Gastrointestinal degradation of Fumonisin B_1 by carboxylesterase FumD prevents Fumonisin induced alteration of sphingolipid metabolism in Turkey and swine. *Toxins (Basel)., 8*, 84. https://doi.org/10.3390/toxins8030084

McCoy, A. J., Grosse-Kunstleve, R. W., Adams, P. D., Winn, M. D., Storoni, L. C., & Read, R. J. (2007). Phaser crystallographic software. *Journal of Applied Crystallography, 40*, 658–674. https://doi.org/10.1107/S0021889807021206

Minekus, M., Alminger, M., Alvito, P., Ballance, S., Bohn, T., Bourlieu, C., Carrière, F., Boutrou, R., Corredig, M., Dupont, D., Dufour, C., Egger, L., Golding, M., Karakaya, S., Kirkhus, B., Le Feunteun, S., Lesmes, U., MacIerzanka, A., MacKie, A., & Brodkorb, A. (2014). A standardised static in vitro digestion method suitable for food-an international consensus. *Food and Function, 5*(6), 1113–1124. https://doi.org/10.1039/c3fo60702j

Mirdita, M., Schütze, K., Moriwaki, Y., Heo, L., Ovchinnikov, S., & Steinegger, M. (2022). ColabFold: Making protein folding accessible to all. *Nature Methods, 19*, 679–682. https://doi.org/10.1038/s41592-022-01488-1

Neckermann, K., Antonissen, G., Doupovec, B., Schatzmayr, D., Gathumbi, J., Delcenserie, V., Uhlig, S., & Croubels, S. (2022). Efficacy of Fumonisin esterase in piglets as animal model for Fumonisin detoxification in humans: Pilot study comparing intraoral to Intragastric administration. *Toxins (Basel)., 14*, 136. https://doi.org/10.3390/toxins14020136

O'Boyle, N., Banck, M., James, C. A., Morley, C., Vandermeersch, T., & Hutchison, G. R. (2011). Open babel: An open chemical toolbox. *Journal of Cheminformatics, 3*, 33. https://doi.org/10.1186/1758-2946-3-33; (Open Babel, Version 2.3.2)

Pereira, C. L., Chen, Y.-H., & McDonald, F. E. (2009). Total synthesis of the sphingolipid biosynthesis inhibitor Fumonisin B_1. *Journal of the American Chemical Society, 131*, 6066–6067. https://doi.org/10.1021/ja9009265

R Core Team. (2021). *R: A language and environment for statistical computing*. Vienna, Austria: R Foundation for Statistical Computing. https://www.R-project.org/.

Reichardt, C., & Welton, T. (2010). *Solvents and solvent effects in organic chemistry; Wiley-VCH Verlag GmbH & co*. KGaA: Weinheim, Germany. https://doi.org/10.1002/9783527632220

Rheeder, J. P., Marasas, W. F. O., & Vismer, H. F. (2002). Production of Fumonisin analogs by fusarium species. *Applied and Environmental Microbiology, 68*, 2001–2005. https://doi.org/10.1128/AEM.68.5.2101-2105.2002

Riley, R. T., & Merrill, A. H. (2019). Ceramide synthase inhibition by fumonisins: A perfect storm of perturbed sphingolipid metabolism, signaling, and disease. *Journal of Lipid Research, 60*, 1183–1189. https://doi.org/10.1194/jlr.S093815

Ritz, C., Baty, F., Streibig, J. C., & Gerhard, D. (2015). Dose-response analysis using R. *PLoS One, 10*, Article e0146021. https://doi.org/10.1371/journal.pone.0146021

Rosignoli, S., & Paiardini, A. (2022). DockingPie: A consensus docking plugin for PyMOL. *Bioinformatics, 38*, 4233–4234. https://doi.org/10.1093/bioinformatics/btac452; DockingPie (Version 1.2.1)

Schwartz-Zimmermann, H. E., Hartinger, D., Doupovec, B., Gruber-Dorninger, C., Aleschko, M., Schaumberger, S., … Moll, W. D. (2018). Application of biomarker methods to investigate FUMzyme mediated gastrointestinal hydrolysis of Fumonisins in pigs. *World Mycotoxin Journal, 11*, 201–214. https://doi.org/10.3920/WMJ2017.2265

Shephard, G. S., Thiel, P. G., Sydenham, E. W., Vleggaar, R., & Alberts, J. F. (1994). Determination of the mycotoxin fumonisin B_1 and identification of its partially hydrolysed metabolites in the faeces of non-human primates. *Food Chemistry and Toxicology, 32*(1), 23–29. https://doi.org/10.1016/0278-6915(84)90032-2

Showalter, S. A., & Brüschweiler, R. (2007). Validation of molecular dynamics simulations of biomolecules using NMR spin relaxation as benchmarks: Application to the AMBER99SB force field. *Journal of Chemical Theory and Computation, 3*, 961–975. https://doi.org/10.1021/ct7000045

Spiller, B., Gershenson, A., Arnold, F. H., & Stevens, R. C. (1999). A structural view of evolutionary divergence. *Proceedings of the National Academy of Sciences U.S.A., 96*(22), 12305–12310. https://doi.org/10.1073/pnas.96.22.12305

Sydenham, E. W., Stockenstrom, S., Thiel, P. G., Shephard, G. S., Koch, K. R., & Marasas, W. F. O. (1995). Potential of alkaline hydrolysis for the removal of Fumonisins from contaminated corn. *Journal of Agricultural and Food Chemistry, 43*(5), 1198–1201. https://doi.org/10.1021/jf00053a014

Sydenham, E. W., Thiel, P. G., Shephard, G. S., Koch, K. R., & Hutton, T. (1995). Preparation and isolation of the partially hydrolyzed moiety of Fumonisin B_1. *Journal of Agricultural and Food Chemistry, 43*(9), 2400–2405. https://doi.org/10.1021/jf00057a016

Trott, O., & Olson, A. J. (2010). AutoDock Vina: Improving the speed and accuracy of docking with a new scoring function, efficient optimization, and multithreading. *Journal of Computational Chemistry, 31*, 455–461. https://doi.org/10.1002/jcc.21334

Vonrhein, C., Flensburg, C., Keller, P., Sharff, A., Smart, O., Paciorek, W., Womack, T., & Bricogne, G. (2011). Data processing and analysis with the AutoPROC toolbox. *Acta Crystallographica Section D Structural Biology, D67*, 293–302. https://doi.org/10.1107/S0907444911007773

Wang, X., Liu, K., Wang, Y., Huang, Z., & Wang, X. (2022). Preparation of 2-Arachidonoylglycerol by enzymatic Alcoholysis: Effects of solvent and water activity on acyl migration. *Foods, 11*, 3213. https://doi.org/10.3390/foods11203213

WHO. (2023). Mycotoxins. https://www.who.int/news-room/fact-sheets/detail/mycotoxins (Fact sheet, 2 October 2023).

Wickham, H. (2023). Modelr: Modelling functions that work with the pipe. *R package, version, 0*(1), 11. https://modelr.tidyverse.org.

Younus, F., Fraser, N. J., Coppin, C. W., Liu, J. W., Correy, G. J., Chertemps, T., … Oakeshott, J. G. (2017). Molecular basis for the behavioral effects of the odorant degrading enzyme esterase 6 in Drosophila. *Scientific Reports, 7*, 46188. https://doi.org/10.1038/srep46188

Zhang, Z., Fang, Q., Xie, T., & Gong, X. (2024). Mechanism of ceramide synthase inhibition by fumonisin B_1. *Structure, 32*(9), 1419–1428. https://doi.org/10.1016/j.str.2024.06.002